

5.4

ESD-TR-80-151

**LEVEL**

12

AD A094075

3

**Solid State Research**

**1980**

**DTIC**  
ELECTRONIC  
JAN 23 1981

Prepared  
under Electronic Systems Division Contract F19628-80-C-0002 by

**Lincoln Laboratory**

MASSACHUSETTS INSTITUTE OF TECHNOLOGY

LEXINGTON, MASSACHUSETTS



C

Approved for public release; distribution unlimited.

DDC FILE COPY

81 1 23 069

The work reported in this document was performed at Lincoln Laboratory, a center for research operated by Massachusetts Institute of Technology, with the support of the Department of the Air Force under Contract F19628-80-C-0002.

This report may be reproduced to satisfy needs of U.S. Government agencies.

The views and conclusions contained in this document are those of the contractor and should not be interpreted as necessarily representing the official policies, either expressed or implied, of the United States Government.

This technical report has been reviewed and is approved for publication.

FOR THE COMMANDER

*Raymond L. Loiselle*  
Raymond L. Loiselle, Lt. Col., USAF  
Chief, ESD Lincoln Laboratory Project Office

Non-Lincoln Recipients  
**PLEASE DO NOT RETURN**  
Permission is given to destroy this document  
when it is no longer needed.

MASSACHUSETTS INSTITUTE OF TECHNOLOGY  
LINCOLN LABORATORY

SOLID STATE RESEARCH

QUARTERLY TECHNICAL SUMMARY REPORT

1 MAY - 31 JULY 1980

ISSUED 7 NOVEMBER 1980

Approved for public release; distribution unlimited.

LEXINGTON

MASSACHUSETTS

DTIC  
JAN 23 1981

**ABSTRACT**

This report covers in detail the solid state research work of the Solid State Division at Lincoln Laboratory for the period 1 May through 31 July 1980. The topics covered are Solid State Device Research, Quantum Electronics, Materials Research, Microelectronics, and Analog Device Technology. Funding is primarily provided by the Air Force, with additional support provided by the Army, DARPA, Navy, NASA, NSF, and DOE.

Accession For		
NTIS GRA&I	<input checked="" type="checkbox"/>	
DTIC TAB	<input type="checkbox"/>	
Unannounced	<input type="checkbox"/>	
Justification	<input type="checkbox"/>	
By _____		
Distribution/		
Availability Codes		
Dist	Avail and/or	Special
A		

## CONTENTS

Abstract	iii
Introduction	vii
Reports on Solid State Research	xi
Organization	xviii
I. SOLID STATE DEVICE RESEARCH	1
A. Avalanche Multiplication and Noise Characteristics of Low-Dark-Current GaInAsP/InP Avalanche Photodetectors	1
B. The Recycling of Spontaneous Photons in GaInAsP/InP Double Heterostructure Lasers	4
C. High-Performance Elevated-Temperature Photomixers for CO <sub>2</sub> Laser Systems	7
II. QUANTUM ELECTRONICS	11
A. Q-Switching and Mode-Locking of Transition Metal Lasers	11
B. Semiconductor Optical Nonlinearities	14
1. Valence Electronic Background	15
2. Carrier Nonparabolicity	15
3. Optical Carrier Generation Effects	16
4. Carrier Redistribution Effects	16
C. Field Operation of a Submillimeter Heterodyne Radiometer	17
III. MATERIALS RESEARCH	21
A. Crystal Growth of InP by the LEC Technique	21
B. Phase Diagram for LPE Growth of GaInAsP Layers Lattice-Matched to InP Substrates	24
C. Vapor-Phase Epitaxy of GaInAsP Alloys on InP Substrates	27
D. Heteroepitaxy of Ge <sub>1-x</sub> Si <sub>x</sub> on Si by Transient Heating of Ge-Coated Substrates	30
E. Liquidus Isotherms, Solidus Lines, and LPE Growth in the Te-Rich Corner of the Hg-Cd-Te System	33
IV. MICROELECTRONICS	39
A. Spatial-Period-Division	39
B. Charge-Coupled Devices: SAW Time-Integrating Correlator with CCD Readout	41
C. High Performance Quasi-Optical GaAs Monolithic Mixer at 110 GHz	43
D. Lateral Epitaxial Overgrowth of Silicon on SiO <sub>2</sub>	44
V. ANALOG DEVICE TECHNOLOGY	49
A. Analog MNOS Memory: Model and Experiments	49
B. LiNbO <sub>3</sub> Surface-Acoustic-Wave Edge-Bonded Transducers on ST Quartz and <001>-Cut GaAs	53
C. An Acoustoelectric Burst-Waveform Processor	57

## INTRODUCTION

### I. SOLID STATE DEVICE RESEARCH

Improved versions of inverted-mesa  $n^+$ -InP/n-GaInAsP/n-InP/ $p^+$ -InP avalanche photodiode structures have been fabricated and characterized. Uniform avalanche gains of 700, dark current densities of  $3 \times 10^{-6}$  A/cm<sup>2</sup> at a multiplication (M) of 10, and an excess noise factor of 3 (also at M = 10) have been achieved in diodes with wavelength cutoff at 1.25  $\mu$ m.

A theoretical analysis shows that, under general conditions in broad-area InGaAsP/InP double-heterostructure lasers, an appreciable amount of reabsorption of the spontaneous photons can occur which results in a lowering of the laser threshold current density. Based on these calculations, improved results can be expected if the free-carrier absorption in the InP and the transmission loss through the laser sidewalls are minimized and/or the absorption in the active layer is enhanced.

P-type HgCdTe photoconductors, which can be operated by thermoelectric cooling, have been investigated for use above 77 K as photo-mixers in tactical CO<sub>2</sub>-laser systems. The devices (100  $\mu$ m square) have shown heterodyne sensitivities at 38 MHz of  $5 \times 10^{-20}$  W/Hz at 77 K and  $1.8 \times 10^{-19}$  W/Hz at 195 K, with bandwidths of 140 and 30 MHz, respectively. Bandwidths in excess of 100 MHz at 195 K were achieved with sensitivities of about  $4 \times 10^{-19}$  W/Hz.

### II. QUANTUM ELECTRONICS

The first observations of tunable Q-switched operation in Ni:MgF<sub>2</sub> and Co:MgF<sub>2</sub> lasers have been made. In addition, the first mode-locked Ni:MgF<sub>2</sub> laser has been demonstrated and has produced pulses of approximately 100 psec duration.

An analysis of mechanisms giving rise to the nonlinear optical response of semiconductors has been developed. Resonance enhancement effects are identified, and the application to bistability in integrated optical devices is discussed.

A number of modifications made on the quasi-optical radiometer has resulted in an improvement in the system noise temperature to 2900 K. The radiometer was used in the detection of CO in the molecular cloud Orion at 691 GHz, marking the first successful submillimeter heterodyne radio astronomy experiment using an optically pumped far-IR laser local oscillator.

### III. MATERIALS RESEARCH

A growth procedure has been developed for using the liquid-encapsulated Czochralski technique to obtain a high yield of InP single crystals capable of providing substrates

for research on optoelectronic devices. By establishing a suitable temperature gradient at the growth interface, this procedure minimizes the probability of twinning but does not result in excessive dislocation densities.

In connection with the liquid-phase-epitaxial growth of GaInAsP/InP heterostructures for optoelectronic devices, the phase diagram for growth of GaInAsP layers lattice-matched to (100) and (111)B InP substrates has been established over the temperature range from 570° to 650°C for the entire composition range from InP to the limiting ternary alloy,  $\text{Ga}_{0.47}\text{In}_{0.53}\text{As}$ . For a given growth temperature and Ga concentration in the liquid phase, the Ga distribution coefficient is always higher for (100) growth than for (111)B growth, but the difference decreases with increasing temperature.

The feasibility of using the trichloride method of vapor-phase-epitaxial growth to obtain GaInAsP/InP heterostructures has been demonstrated by growing lattice-matched GaInAsP layers on (100) InP substrates. Further development of this method, which uses  $\text{PCl}_3$  and  $\text{AsCl}_3$  as the sources of the Group V elements, would be required to achieve the degree of alloy composition control desired for device applications.

Heteroepitaxial  $\text{Ge}_{1-x}\text{Si}_x$  alloy films of good crystal quality have been obtained by transient heating of Ge-coated Si single-crystal samples with a graphite strip-heater. On the basis of initial experiments on the chemical vapor deposition of GaAs layers on these alloy films, there appear to be no serious obstacles to the fabrication of high-efficiency, low-cost GaAs solar cells utilizing the GaAs/ $\text{Ge}_{1-x}\text{Si}_x$ /Si structure.

Liquidus isotherms for temperatures from 425° to 600°C and solidus lines for CdTe mole fractions between 0 and 0.7 have been determined for the Te-rich corner of the Hg-Cd-Te system. From the data, it is clear that a very wide range of  $\text{Hg}_{1-x}\text{Cd}_x\text{Te}$  compositions can be grown at temperatures of 425° to 600°C by liquid-phase-epitaxial techniques.

#### IV. MICROELECTRONICS

A simple technique has been developed for exposing large-area, low-distortion, periodic structures. The technique, called spatial-period-division, employs near-field diffraction from periodic and quasi-periodic parent masks to produce intensity patterns with spatial periods finer than the parent mask. Spatial-period-division used in conjunction with soft x-ray lithography should be especially attractive for exposing structures with periods below 100 nm.

Two schemes have been implemented for fixed-pattern-noise cancellation in a SAW/CCD time-integrating correlator. One method uses a second CCD chip to store the fixed-pattern noise for subsequent subtraction from the SAW/CCD output, and the other uses an A/D converter and a computer for digital post-processing of the correlator output. The dynamic range of the device has been improved to 40 dB from 20 dB.

A GaAs integrated mixer consisting of a slot coupler, a coplanar transmission line, a surface-oriented Schottky-barrier diode, and an RF bypass capacitor all monolithically integrated on the GaAs surface has been fabricated for operation at 110 GHz. The monolithic mixer module mounted in the end of a waveguide horn has an uncooled double-sideband mixer noise temperature of 339 K and a conversion loss of 3.8 dB.

Lateral overgrowth of single-crystal Si over an SiO<sub>2</sub> bar structure on a single-crystal silicon substrate has been achieved by epitaxial growth using the reduction of silane in a hydrogen gas environment. Up to 4 μm of lateral overgrowth has been observed for thin (<0.03 μm) SiO<sub>2</sub> bars on (100)-oriented silicon wafers. The amount of overgrowth is dependent on the orientation of the silicon substrate and the thickness of the SiO<sub>2</sub> layer.

#### V. ANALOG DEVICE TECHNOLOGY

A theoretical model has been developed which explains an earlier experimental demonstration of analog nonvolatile memory in metal-nitride-oxide-semiconductor (MNOS) capacitors. Experiments have successfully extended such analog memory behavior to devices produced by a process compatible with charge-coupled-device (CCD) technology. These results indicate the feasibility of an integrated MNOS/CCD analog memory, and work to fabricate such a memory is now under way.

LiNbO<sub>3</sub> surface-acoustic-wave edge-bonded transducers have been fabricated on ST quartz and <001>-cut GaAs substrates. Efficient transduction has been demonstrated in the vicinity of 100 MHz with fractional bandwidths of 50 and 91 percent for the quartz and GaAs substrates, respectively. Conversion loss as low as 4 dB has been measured for quartz. A model which accurately predicts this transducer performance has been devised.

Recent experiments have demonstrated the feasibility of using an acoustoelectric coherent integrator for programmable processing of burst waveforms of the type employed in Doppler radar systems. The device output, as a function of Doppler-shifted input, produced the expected Doppler ambiguity functions for 3-μsec gated-CW subpulses in bursts of 2, 4, 8, 16, and 32 subpulses.

DIVISION 8  
REPORTS ON SOLID STATE RESEARCH

15 May through 15 August 1980

PUBLISHED REPORTS

Journal Articles

<u>JA No.</u>			
4947	Solid Electrolytes Containing Both Mobile and Immobile Alkali Ions	H. Y-P. Hong	J. Power Sources <u>5</u> , 137 (1980)
5019	Doppler-Limited Spectroscopy of the $3\nu_3$ Band of SF <sub>6</sub>	A. S. Pine A. G. Robiette*	J. Mol. Spectrosc. <u>80</u> , 388 (1980)
5033	The Growth of Large, Laser Quality Nd <sub>x</sub> RE <sub>1-x</sub> P <sub>5</sub> O <sub>14</sub> Crystals	R. D. Plattner* W. W. Krühler* W. K. Zwickler* T. Kovats* S. R. Chinn	J. Cryst. Growth <u>49</u> , 274 (1980)
5043	Pump Depletion and Saturation of Two-Photon Resonant Third-Harmonic Generation Processes	H. Kildal S. R. J. Brueck	IEEE J. Quantum Electron. <u>QE-16</u> , 566 (1980)
5049	Deconvolution of Infrared Spectra Beyond the Doppler Limit	J. Pliva* A. S. Pine P. D. Willson*	Appl. Opt. <u>19</u> , 1833 (1980)
5052	Fabrication and Numerical Simulation of the Permeable Base Transistor	C. O. Bozler G. D. Alley	IEEE Trans. Electron Devices <u>ED-27</u> , 1128 (1980)
5057	Observation of Stimulated Level Shifting in Inverted Atomic Thallium Populations	D. J. Ehrlich R. M. Osgood, Jr. A. Sanchez	Phys. Rev. Lett. <u>44</u> , 871 (1980)
5065	Ohmic Contact Formation on InP by Pulsed Laser Photochemical Doping	T. F. Deutsch D. J. Ehrlich R. M. Osgood, Jr. Z. L. Liao	Appl. Phys. Lett. <u>36</u> , 847 (1980)
5067	X-Ray Lithography - A Review and Assessment of Future Applications	H. I. Smith D. C. Flanders	J. Vac. Sci. Technol. <u>17</u> , 533 (1980)
5068	Direct Writing of Regions of High Doping on Semiconductors by UV-Laser Photodeposition	D. J. Ehrlich R. M. Osgood, Jr. T. F. Deutsch	Appl. Phys. Lett. <u>36</u> , 916 (1980)

\* Author not at Lincoln Laboratory.

JA No.

- |      |  |  |  |
|------|--|--|--|
| 5074 | One-Step Repair of Transparent Defects in Hard-Surface Photolithographic Masks via Laser Photodeposition | D. J. Ehrlich<br>R. M. Osgood, Jr.<br>D. J. Silversmith<br>T. F. Deutsch | IEEE Electron. Devices Lett. EDL-1, 101 (1980)       |
| 5087 | Far Infrared Heterodyne Detectors  | P. E. Tannenwald   | Intl. J. Infrared and Millimeter Waves 1, 159 (1980) |
| 5093 | High-Temperature cw Operation of GaInAsP/InP Lasers Emitting at 1.5 $\mu\text{m}$                        | J. J. Hsieh  | Appl. Phys. Lett. 37, 25 (1980)                      |
| 5108 | High-Speed Operation of LiNbO <sub>3</sub> Electro-optic Interferometric Waveguide Modulators            | F. J. Leonberger   | Opt. Lett. 5, 312 (1980)                             |
| 5110 | Optically Pumped Ce:LaF <sub>3</sub> Laser at 286 nm   | D. J. Ehrlich<br>P. F. Moulton<br>R. M. Osgood, Jr.                      | Opt. Lett. 5, 339 (1980)                             |

Meeting Speeches

MS No.

- |       |   |   |  |
|-------|---|---|--|
| 5044A | 1.0-1.6 $\mu\text{m}$ Sources and Detectors for Fiber Optics Applications   | A. G. Foyt  | Proc. Intl. Conf. on Lasers '79, Orlando, Florida, 17-21 December 1979, pp. 410-416  |
| 5124  | Proposed Design of a-Si:H Solar Cells Using Ultrathin Active Layer to Increase Conversion Efficiency                                    | J. C. C. Fan<br>C. O. Bozler  | Proc. Fourteenth IEEE Photovoltaic Specialists Conference - 1980, San Diego, California, 7-10 January 1980, pp. 1070-1073              |
| 5127  | GaAs Shallow-Homojunction Solar Cells   | J. C. C. Fan<br>G. W. Turner<br>R. P. Gale<br>C. O. Bozler                                  | Proc. Fourteenth IEEE Photovoltaic Specialists Conference - 1980, San Diego, California, 7-10 January 1980, pp. 1102-1105              |
| 5130  | A New Technique for Producing Large-Grained Semiconductor Sheets by Laser Crystallization of Amorphous Films                            | J. C. C. Fan<br>H. J. Zeiger<br>R. P. Gale<br>R. L. Chapman                                 | Proc. Fourteenth IEEE Photovoltaic Specialists Conference - 1980, San Diego, California, 7-10 January 1980, pp. 218-223                |
| 5154  | Fabrication of Ohmic Contacts on p-Type InP Using Ion Implantation and Laser Annealing  | Z. L. Liao<br>N. L. DeMeo<br>J. P. Donnelly<br>D. E. Mull<br>R. Bradbury*<br>J. P. Lorenzo* | In <u>Laser and Electron Beam Processing of Materials</u> , C. W. White and P. S. Percy, Eds. (Academic Press, New York, 1980), p. 494 |
| 5157  | Solid-Phase Crystallization Produced by Laser Scanning of Amorphous Ge Films: The Role of Latent Heat in Crystallization Front Dynamics | H. J. Zeiger<br>J. C. C. Fan<br>R. P. Gale<br>R. L. Chapman                                 | In <u>Laser and Electron Beam Processing of Materials</u> , C. W. White and P. S. Percy, Eds. (Academic Press, New York, 1980), p. 234 |

\* Author not at Lincoln Laboratory.

MS No.

- |      |  |   |   |
|------|--|---|---|
| 5169 | Redistribution of Implanted Zn in InP After Q-Switched Laser Annealing and the Related Specific Contact Resistance | Z. L. Liao<br>N. L. DeMeo<br>J. P. Donnelly*<br>J. C. Norberg*<br>C. G. Hopkins*<br>C. A. Evans, Jr.*<br>J. P. Lorenzo* | In <u>Laser and Electron Beam Processing of Materials</u> , C. W. White and P. S. Peercy, Eds. (Academic Press, New York, 1980), p. 500 |
|------|--|---|---|

\* \* \* \* \*

UNPUBLISHED REPORTS

Journal Articles

JA No.

- |      |   |  |  |
|------|---|--|--|
| 5072 | Photo-Acoustic and Photo-Refractive Detection of Small Absorptions in Liquids                       | S. R. J. Brueck<br>H. Kildal<br>L. J. Belanger                                       | Accepted by Opt. Commun.   |
| 5076 | Formation of the XeBr Exciplex by Xe-Br <sub>2</sub> (D') Collisions                                | D. J. Ehrlich<br>R. M. Osgood, Jr.   | Accepted by J. Chem. Phys.   |
| 5083 | Laser Micro-Photochemistry for Use in Solid State Electronics                                       | D. J. Ehrlich<br>R. M. Osgood, Jr.<br>T. F. Deutsch                                  | Accepted by IEEE J. Quantum Electron.  |
| 5103 | Remote Sensing of NO Using a Differential Absorption LIDAR  | N. Menyuk<br>D. K. Killinger<br>W. E. DeFeo  | Accepted by Appl. Opt.   |
| 5111 | Infrared Spectroscopy Using Tunable Lasers  | H. R. Schlossberg*<br>P. L. Kelley   | Accepted as Chapter 4 in <u>Spectrometric Techniques</u> , Vol. 2, G. A. Vanasse, Ed. (Academic Press, New York) |
| 5112 | Silicon Graphoepitaxy Using a Strip-Heater Oven   | M. W. Geis<br>D. A. Antoniadis<br>D. J. Silversmith<br>R. W. Mountain<br>H. I. Smith | Accepted by Appl. Phys. Lett.  |
| 5115 | Surface Passivation Techniques for InP and InGaAsP p-n Junction Structures                          | V. Diadiuk<br>C. A. Armiento<br>S. H. Groves<br>C. E. Hurwitz                        | Accepted by IEEE Electron. Devices Lett.   |
| 5119 | The CLEFT Process, A Technique for Producing Epitaxial Films on Reusable Substrates                 | R. W. McClelland<br>C. O. Bozler<br>J. C. C. Fan                                     | Accepted by Appl. Phys. Lett.  |
| 5123 | Orientational and Electronic Contributions to the Third-Order Susceptibilities of Cryogenic Liquids | H. Kildal<br>S. R. J. Brueck   | Accepted by J. Chem. Phys.   |

\* Author not at Lincoln Laboratory.

JA No.

5135	High Performance Quasi-Optical GaAs Monolithic Mixer at 110 GHz	B. J. Clifton G. D. Alley R. A. Murphy I. H. Mroczkowski	Accepted by IEEE Trans. Electron Devices
------	---	---	--

Meeting Speeches \*

MS No.

4530D	High-Resolution Molecular Spectroscopy Using a Tunable Difference-Frequency Laser System	A. S. Pine	High Resolution Infrared Applications and Developments Symp., Gaithersburg, Maryland, 23-25 June 1980
4967B	Graphoepitaxy	D. C. Flanders	Greater New York Chapter American Vacuum Society, RCA Laboratories, Princeton, New Jersey, 4 June 1980
5127A	Recent Advances in High Efficiency, Low Cost GaAs Solar Cells	J. C. C. Fan G. W. Turner R. P. Gale C. O. Bozler	1980 Gordon Research Conference on Crystal Growth, Plymouth, New Hampshire, 14-18 July 1980
5130A	Laser Processing of Semiconductors	J. C. C. Fan H. J. Zeiger R. P. Gale R. L. Chapman	Seminar, Digital Equipment Corporation, Hudson, Massachusetts, 11-12 June 1980
5157A	Solid-Phase Crystallization Produced by Laser Scanning of Amorphous Ge Films: The Role of Latent Heat in Crystallization Front Dynamics	H. J. Zeiger J. C. C. Fan R. P. Gale R. L. Chapman	
5204A	Low Loss GaAs Optical Waveguides Formed by Lateral Epitaxial Growth over Oxide	F. J. Leonberger C. O. Bozler R. W. McClelland I. Melngailis	
5325	Analog Memory in MNOS Devices: Model and Experiments	R. S. Withers R. W. Ralston E. Stern	38th Annual Device Research Conference, Cornell University, Ithaca, New York, 23-25 June 1980
5334	Low Leakage, High Gain GaInAsP/InP Avalanche Photodetectors	V. Diadiuk S. H. Groves C. E. Hurwitz	
5335	Intracavity-Loss-Modulated GaInAsP Diode Lasers	D. Z. Tsang J. N. Walpole S. H. Groves J. J. Hsieh J. P. Donnelly	

\* Titles of Meeting Speeches are listed for information only. No copies are available for distribution.

<u>MS No.</u>			
5346	Direct Writing of Micrometer-Sized, Highly Doped Regions on Semiconductors by UV-Laser Photodeposition	D. J. Ehrlich R. M. Osgood, Jr. T. F. Deutsch	} 38th Annual Device Research Conference, Cornell University, Ithaca, New York, 23-25 June 1980
5358	The CLEFT Process: A Technique for Producing Many Single-Crystal Films of GaAs from One Reusable Substrate	R. W. McClelland C. O. Bozler J. C. C. Fan	
5219A	Integrated Optics and Optoelectronic Switches for Signal Processing	F. J. Leonberger	Workshop on High-Speed Optical and Electronic Devices, Dedham, Massachusetts, 21 June 1980
5232	High-Power Output and Tuning Properties of the UV Solid-State Ce:YLF Laser	D. J. Ehrlich P. F. Moulton R. M. Osgood, Jr.	} XI Intl. Quantum Electronics Conference, Boston, 23-26 June 1980
5236	Laser-Induced Photochemical Reactions for Electronic-Device Fabrication	D. J. Ehrlich R. M. Osgood, Jr. T. F. Deutsch	
5237	Recent Advances in Transition-Metal-Doped Lasers	P. F. Moulton A. Mooradian	
5245	Temperature-Dependent Spectral Study of the XeBr Excimer Bands via Two-Photon Optical Pumping	D. J. Ehrlich R. M. Osgood, Jr.	
5373	The $n\nu_3$ Multiple-Photon Ladder of SF <sub>6</sub>	C. W. Patterson* R. S. McDowell* P. F. Moulton A. Mooradian	
5234	Submicrometer Technology and Devices for VLSI	W. T. Lindley	} Electro '80, Boston, 12-15 May 1980
5352	Monolithic Circuit Design	A. Chu	
5236A	Laser-Induced Photochemical Reactions for Electronic-Device Fabrication	D. J. Ehrlich R. M. Osgood, Jr. T. F. Deutsch	Gordon Research Conference, Meriden, New Hampshire, 21-25 June 1980
5243	A Review of X-Ray Lithography	H. I. Smith D. C. Flanders	9th Intl. Conf. on Electron and Ion Beam Science and Technology, St. Louis, Missouri, 11-16 May 1980
5264, 5264B	Recent Advances in Tunable Lasers	A. Mooradian	Intl. Conf. on Lasers, Peking, China, 19-22 May 1980; Seminar, Raytheon Co., Waltham, Massachusetts, 11 June 1980

\* Author not at Lincoln Laboratory.

<u>MS No.</u>			
5264A	Recent Advances in Tunable Lasers	A. Mooradian	} Sergio Porto Memorial Conference on Lasers and Applications, Rio de Janeiro, Brazil, 29 June - 3 July 1980
5394	Nonlinear Optics of Cryogenic Liquids	S. R. J. Brueck H. Kildal	
5271	Vapor-Phase Epitaxy of InP and GaInAsP	P. Vohl	} NATO-sponsored Workshop on InP, Harwichport, Massachusetts, 17-19 June 1980
5285	Synthesis and Crystal Growth of InP	G. W. Iseler	
5324	Liquid-Phase Epitaxial Growth of InP and InGaAsP Alloys	S. H. Groves M. C. Plonko	
5370	The Electro-optic Applications of InP	A. G. Foyt	
5278B	Silicon Graphoepitaxy	M. W. Geis D. C. Flanders D. J. Silversmith D. A. Antoniadis H. I. Smith	Solar Energy Research Institute - Program Review Talk, Washington, DC, 10-12 June 1980
5278C	Graphoepitaxy of Silicon	M. W. Geis	} Gordon Research Conference, New London, New Hampshire, 23-25 June 1980
5411	Research at the Limits of Microstructure Fabrication	D. C. Flanders	
5294	Collisional Narrowing of HF Fundamental Band Spectral Lines by Neon and Argon	A. S. Pine	35th Annual Symposium on Molecular Spectroscopy, Ohio State University, Columbus, 16-20 June 1980
5312	Extending the Operating Temperature, Wavelength and Frequency Response of HgCdTe Heterodyne Detectors	D. L. Spears	Intl. Conf. on Heterodyne Systems and Technology, Williamsburg, Virginia, 25-27 March 1980
5320	Surface Diffusion in MBE Growth of GaAs	A. R. Calawa	} Electronic Materials Conference, Cornell University, Ithaca, New York, 24-27 June 1980
5321	Phase Diagram for LPE Growth of GaInAsP Layers Lattice-Matched to InP Substrates	J. J. Hsieh	
5322	Properties of W-GaAs Schottky Barriers After High Temperature Anneal	K. B. Nichols C. O. Bozler	
5327	Growth-Temperature Dependence of LPE GaInAsP/InP Lattice Mismatch	Z. L. Liao J. J. Hsieh	
5349	DIAL Measurements of C <sub>2</sub> H <sub>4</sub>	D. K. Killinger N. Menyuk	Topical Meeting on Coherent Laser Radar for Atmospheric Sensing, Aspen, Colorado, 15-17 July 1980

MS No.

5385	Surface-Acoustic-Wave Chirp-Fourier-Transform Techniques for Doppler Signal Processing in Laser Radars	R. C. Williamson J. T. Lynch D. R. Arsenault V. S. Dolat	Topical Meeting on Coherent Laser Radar for Atmospheric Sensing, Aspen, Colorado, 15-17 July 1980
5369	The Electrical Characteristics of Ion Implanted Compound Semiconductors	J. P. Donnelly	IBMM-80 Conference on Ion Beam Modification of Materials, Albany, New York, 14-18 July 1980
5371	Reactive Ion Etching of Superconducting Devices	S. A. Reible	New England Chapter American Vacuum Society Symp., Danvers, Massachusetts, 17 June 1980
5380	Systems Aspects of SAW Convolvers	J. H. Cafarella	1980 Intl. Microwave Symp., Washington, DC, 28-30 May 1980
5458	Signal Processing with Acoustoelectric SAW Devices	I. Yao	SPIE Annual Intl. Conf., San Diego, California, 29-31 July 1980

## ORGANIZATION

### SOLID STATE DIVISION

A. L. McWhorter, *Head*  
I. Melngailis, *Associate Head*  
J. F. Goodwin, *Assistant*  
R. H. Rediker, *Senior Staff*  
P. E. Tannenwald, *Senior Staff*

### QUANTUM ELECTRONICS

A. Mooradian, *Leader*  
P. L. Kelley, *Associate Leader*

Barch, W. E.	Fleming, M. W.*
Belanger, I. J.	Goodhue, W. D.*
Blumberg, W. A. M.	Hancock, R. C.
Brucek, S. R. J.	Kildal, H.
Burke, J. W.	Killinger, D.
Bushee, J. F.	Menyuk, N.
Chinn, S. R.	Moulton, P. F.
DeFeo, W. E.	Osgood, R. M., Jr.
Deutsch, T. F.	Parker, C. D.
Ehrlich, D. J.	Peck, D. D.
Feldman, B.	Pine, A. S.
Fetterman, H. R.	Williams, G. E.*

### ELECTRONIC MATERIALS

A. J. Strauss, *Leader*  
H. J. Zeiger, *Associate Leader*  
J. G. Mavroides, *Senior Staff*

Anderson, C. H., Jr.	Iseler, G. W.
Button, M. J.	Kafalas, J. A.
Chapman, R. L.	Kolesar, D. F.
Davis, F. M.	Krohn, L., Jr.
Delaney, E. J.	Mastromattei, E. L.
Fahey, R. E.	Owens, E. B.
Fan, J. C. C.	Palm, B. J.
Finn, M. C.	Pantano, J. V.
Foley, G. H.	Salerno, J. P.*
Gale, R. P.	Tracy, D. M.
Hong, H. Y-P.	Tsaurs, B-Y.
Hsieh, J. J.	Vohl, P.

### APPLIED PHYSICS

R. C. Williamson, *Leader*  
C. E. Hurwitz, *Associate Leader*  
T. C. Harman, *Senior Staff*  
R. H. Kingston, *Senior Staff*

Anniento, C. A.*	Leonberger, F. J.
Calawa, A. R.	Liau, Z-L.
Carter, F. B.	Lind, T. A.
DeMeo, N. L., Jr.	McBride, W. F.
Diadiuk, V.	Paladino, A. E.
Donnelly, J. P.	Plonko, M. C.
Duffy, P. E.	Spears, D. L.
Ferrante, G. A.	Tsang, D. Z.*
Foyt, A. G.	Turner, G. W.
Groves, S. H.	Walpole, J. N.
Kirsch, S. T.*	

### ANALOG DEVICE TECHNOLOGY

E. Stern, *Leader*  
J. H. Cafarella, *Assistant Leader*  
R. W. Ralston, *Assistant Leader*

Anderson, A. C.	Kernan, W. C.
Arsenault, D. R.	Leung, I.
Baker, R. P.	Lowney, S. D.
Becker, R. A.	Lynch, J. T.
Behrmann, G. J.	Oates, D. E.
Brogan, W. T.	Reible, S. A.
Dolat, V. S.	Slattery, R. L.
Fisher, J. H.	Withers, R. S.
Holtham, J. H.	Yao, I.

### MICROELECTRONICS

W. T. Lindley, *Leader*  
F. J. Bachner, *Associate Leader*  
H. I. Smith, *Assistant Leader*  
R. A. Murphy, *Assistant Leader*

Alley, G. D.	Elta, M. E.	Mahoney, I. J.
Bozler, C. O.	Felton, B. J.	McClelland, R. W.
Burke, B. E.	Flanders, D. C.	Melngailis, J.†
Cabral, S. M.	Geis, M. W.	McGonagle, W. H.
Chiang, A. M.	Goeloe, G. T.‡	Mountain, R. W.
Chu, A.	Gray, R. V.	Nichols, K. H.
Clifton, B. J.	Hansell, G. I.*	Piacentini, W. J.
Daniels, P. J.	Hawryluk, A. M.*	Pichler, H. H.
DeGraff, P. D.	Jacobsen, E. H.	Rathman, D. D.
Durant, G. L.	Lincoln, G. A., Jr.	Shaver, D. C.‡
Economou, N. P.	Lyszczarz, T.	Silversmith, D. J.
Efremow, N., Jr.	Macropoulos, W.	Smythe, D. L., Jr.
		Wilde, R. E.

\*Research Assistant

†Part Time

‡Staff Associate

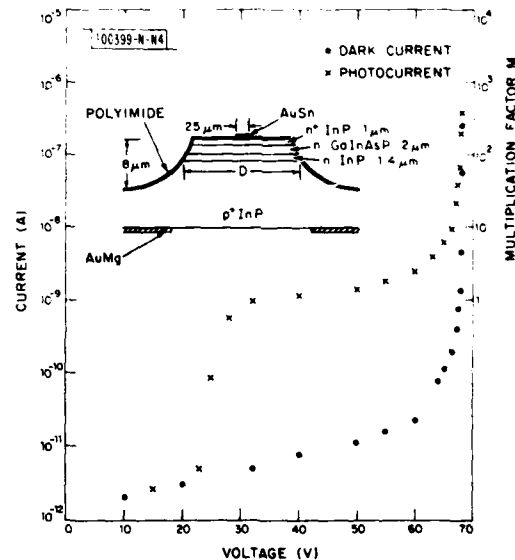
## I. SOLID STATE DEVICE RESEARCH

### A. AVALANCHE MULTIPLICATION AND NOISE CHARACTERISTICS OF LOW-DARK-CURRENT GaInAsP/InP AVALANCHE PHOTODETECTORS

Uniform avalanche gains of 700, dark-current densities of  $3 \times 10^{-6}$  A/cm<sup>2</sup> at  $M = 10$ , and an excess noise factor of  $\sim 3$ , also at  $M = 10$ , have been achieved at wavelengths up to 1.25  $\mu\text{m}$  in improved versions of the inverted-mesa  $n^+ \text{-InP/n-GaInAsP/n-InP/p}^+ \text{-InP}$  photodiode structures described previously.<sup>1</sup> The low dark current results from the placement of the p-n junction in the InP and from the use of a new passivation technique.

The structure, shown in the inset of Fig. I-1, is similar to the earlier one<sup>1</sup> with the exception of the top  $n^+ \text{-InP}$  layer which had been left out in the earlier devices for simplicity. This  $n^+ \text{-InP}$  top layer provides a low-resistance, transparent contact and eliminates losses due to surface recombination. The mesas were fabricated as described previously,<sup>1</sup> with the exception that surface passivation, which was found to be critical to attainment of reproducibly low dark currents, was accomplished by application of a DuPont polyimide<sup>2</sup> film (5-8  $\mu\text{m}$  thick) directly over the freshly etched mesas. The film was patterned using standard photolithographic techniques and cured by baking at 200°C for 1 hour. Devices so passivated were found to be highly stable in normal room atmosphere and under sustained high values of bias voltage.

Fig. I-1. I-V characteristics of GaInAsP/InP APD with  $D = 76.2 \mu\text{m}$ . Photoresponse was taken at 200 Hz using chopped 1.15- $\mu\text{m}$  light and at frequencies ranging from 1 kHz to 25 MHz using the modulated output of a 1.21- $\mu\text{m}$  GaInAsP laser. The multiplication factor was measured with 1 nA of primary photocurrent. Inset: Device structure; device diameters  $D$  varied from 64 to 152  $\mu\text{m}$ .



Typical reverse I-V characteristics with and without light are shown in Fig. I-1. The photocurrent measurement was performed at 200 Hz by illuminating the device with chopped 1.15- $\mu\text{m}$  light from a He-Ne laser, and at frequencies ranging from 1 kHz to 25 MHz by using the modulated output of a 1.21- $\mu\text{m}$  GaInAsP laser. The multiplication vs bias was independent of frequency over this range. Pulse-response rise times of less than 160 psec, measured with an avalanche gain of 40 and limited by the rise time of the mode-locked Nd:YAG laser pulse,

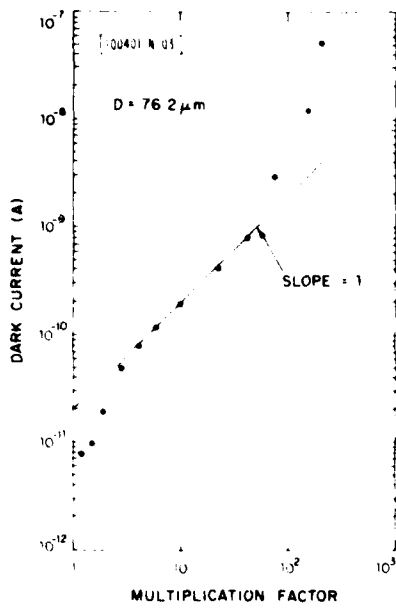
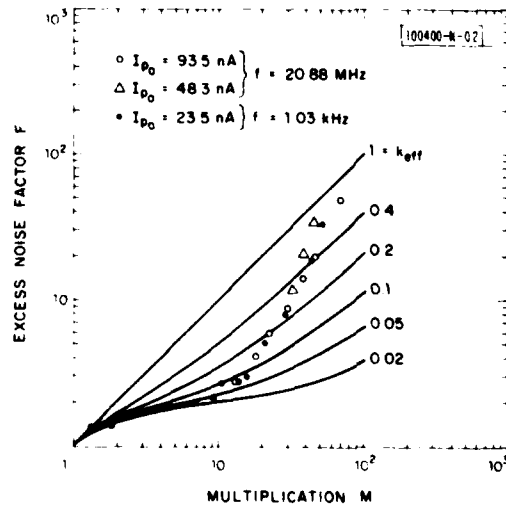


Fig. 1-2. Dark current vs multiplication factor for different applied voltages.

Fig. 1-3. Experimental excess noise factor vs multiplication for several primary photocurrents and frequencies. Solid curves were calculated from the theory of McIntyre<sup>9,10</sup> with  $k_{eff}$  defined as the effective electron-to-hole ionization coefficient ratio.



indicate that the frequency response extends beyond 1 GHz. Based on measurements on conventional versions of GaInAsP/InP photodiodes whose response characteristics should not differ essentially from the present devices, it can be inferred that pulsewidths of <80 psec should be achievable.<sup>3</sup> Photoresponse scans with the light incident from the front or back side showed uniform response and absence of microplasmas. The onset of the photoresponse beginning at about 23 V corresponds to the punch-through of the depletion region from the InP into the GaInAsP. The photogenerated holes, which at low bias had been confined to the GaInAsP by the valence band barrier of the heterojunction, are now swept by the junction field over the barrier into the InP where they are collected.<sup>4,5</sup> This punch-through voltage is in agreement with that obtained from C-V measurements. At all frequencies, the maximum value of photo-multiplication decreased with increasing primary photocurrents over the range of 1 nA to 1  $\mu$ A, in good agreement with the gain-saturation model of Melchior and Lynch.<sup>6</sup> The maximum avalanche multiplication, obtained for an initial photocurrent of 1 nA, was  $\sim$ 700.

In Fig. 1-2, for the same device, the measured dark current at a given bias voltage has been plotted as a function of the photocurrent multiplication factor at that same bias. At low values of multiplication (covering the bias range from about 20 to 60 V), the current rises rapidly as the depletion region spreads into the GaInAsP from the wider-gap InP and the dark current (presumably due to bulk space charge generation) increases and begins to be multiplied. Over the range of multiplication from approximately 2 to 50 (corresponding to a bias range of  $\sim$ 60 to 67 V) the dark current is proportional to the multiplication, indicating that over this range the dominant component of the dark current is bulk space charge generation current which is being multiplied by the avalanche process. At larger values of multiplication (i.e., biases above 67 V) the dark current rises more rapidly than the multiplication, indicating that the electric field in the GaInAsP itself has increased to the point that the anomalous leakage currents (possibly due to tunneling<sup>7</sup>) observed in conventional GaInAsP p-n junction devices become dominant.

Noise measurements as a function of multiplication were made at several frequencies from 200 Hz to 25 MHz and for varying levels of illumination incident from both the front and the back of the detector. A sensitive spectrum analyzer and low-noise transimpedance amplifiers were employed. The excess noise factor<sup>8</sup>  $F$ , calculated from the measured values of noise added by the incident light and the concurrently measured multiplication, is plotted in Fig. 1-3 as a function of multiplication. The solid curves were calculated from the theory of McIntyre, with  $k_{eff}$  defined as the effective electron-to-hole ionization coefficient ratio.<sup>9,10</sup>  $F$  is independent of photocurrent, frequency, and direction of illumination. This result is in qualitative agreement with those obtained in InP,<sup>11</sup> and is consistent with  $\beta > \alpha$ , where  $\beta$  and  $\alpha$  are, respectively, the hole and electron ionization coefficients. (The photogenerated carriers swept into the InP and thence multiplied are purely holes.) As evident from the figure, low values of  $F$ , consistent with a  $k_{eff}$  of 0.02 to 0.1, are found for  $M < 10$ . For larger values of multiplication,  $F$  increases considerably more rapidly than expected. The reason for this result is not known at present. Multiplication in the GaInAsP, for which holes have the lower ionization coefficient,<sup>12</sup> can apparently be ruled out since the maximum field there is less than that at which multiplication is observed in avalanche photodiodes (APDs) with the p-n junction in GaInAsP of the same composition. Similar behavior has been observed<sup>8</sup> in Si APDs, but appears to be dependent on the specific device structure.

The quantum efficiency of the GaInAsP/InP photodiodes measured from the front was 50%, a value which is somewhat lower than the reflection-limited maximum of 70% because of carrier

recombination in the undepleted region of GaInAsP. This can be corrected by optimizing the device parameters during growth. The efficiency for back illumination is low because of free-carrier absorption in the heavily doped p-type substrate. Thinning of the wafer will be required to achieve high quantum efficiencies in this mode.

The GaInAsP/InP APDs reported here are not of optimal design and have noise characteristics at high multiplication which at present are higher than predicted. Nevertheless, it is clear that they already are considerably more sensitive than any competitive devices hitherto reported and promise even higher performance with further development.

V. Diadiuk  
S. H. Groves  
C. E. Hurwitz

#### B. THE RECYCLING OF SPONTANEOUS PHOTONS IN GaInAsP/InP DOUBLE HETEROSTRUCTURE LASERS

A theoretical analysis has been carried out which reveals the significance of the transparency of the InP substrate to the spontaneous light emitted by the GaInAsP active layer in GaInAsP/InP double heterostructure lasers. Because of the metallic contacts and the large difference of the refractive indices between InP and air, the spontaneously emitted photons will bounce around within the device and have a large probability of being reabsorbed by the active layer (via band-to-band transitions). This reabsorption of spontaneous light will be important for the semiconductor lasers, especially for the lowering of the threshold current density.

Figure I-4 shows a schematic drawing of a broad-area GaInAsP/InP double heterostructure (DH) laser diode. Most of the spontaneous light emitted from the active layer will be reflected by the two metallic ohmic contacts (top and bottom in Fig. I-4) and the sidewalls and be confined to the device volume. We will therefore treat the spontaneous light as a photon gas filling the whole device. For simplicity we ignore the absorption at the metallic contacts. There are then three major processes which contribute to the consumption of the spontaneous photons, namely: (1) transmission through the sidewalls of the device, (2) free-carrier absorption in the InP substrate and cladding layers, and (3) reabsorption (band to band) in the active layer. (The total

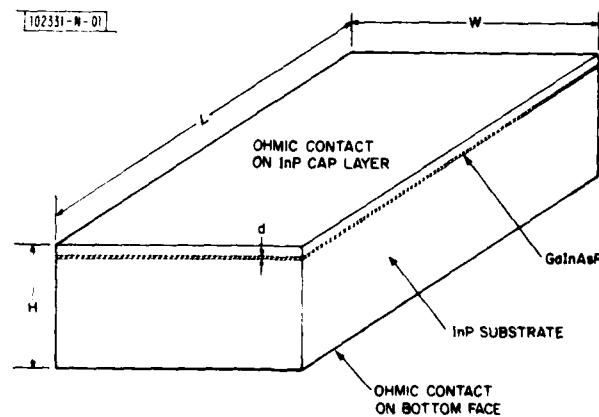


Fig. I-4. Schematic drawing of the broad-area GaInAsP/InP double-heterostructure laser diode used in the present calculation. The shaded region is the GaInAsP active layer. The top and bottom faces ( $L \times W$ ) are the ohmic contacts.

free-carrier absorption in the active layer is small relative to the substrate and cladding layers, since the active layer is generally much thinner.)

Only those photons impinging upon the sidewall within an angle  $< 20^\circ$  (critical angle) of the surface normal can be transmitted into the air.<sup>13</sup> The average transmission probability for photons within this angle per bounce is  $\sim 70\%$ . Therefore the number of photons transmitted into the air per unit time,  $R_t$ , is given by

$$R_t \cong NA \frac{c}{\bar{n}} \times \frac{\Omega}{4\pi} \times 0.70 \quad (I-1)$$

where  $N$  is the photon density (per unit volume) in the device,  $A \cong 2(LH + WH)$  is the total area of the sidewalls (cf. Fig. 1-4),  $c/\bar{n}$  is the speed of light in InP (with  $\bar{n}$  being the refractive index of InP), and  $\Omega$  is the solid angle within which transmission is possible. It can easily be shown that  $\Omega/4\pi = 0.0302$ .

The number of photons absorbed by the free carriers in InP per unit time,  $R_a$ , is given by

$$R_a \cong NV \frac{c}{\bar{n}} \alpha_{\text{InP}} \quad (I-2)$$

where  $V = LWH$  is the total volume of the device and  $\alpha_{\text{InP}}$  is the average free-carrier absorption coefficient of the InP substrate and cladding layers. The number of photons reabsorbed in the active layer per unit time,  $R_r$ , is given by

$$R_r \cong NV \frac{c}{\bar{n}} \frac{d}{H} \bar{\alpha}_Q \quad (I-3)$$

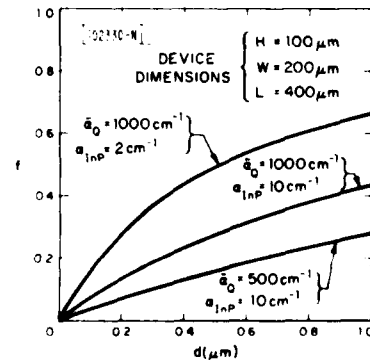
where  $d$  is the active layer thickness (in general,  $d \ll H$ ) and  $\bar{\alpha}_Q$  is the average band-to-band absorption coefficient in the active layer.

The fraction,  $f$ , of the spontaneous photons which is reabsorbed by the active layer is given by  $f \cong R_r / (R_r + R_a + R_t)$ . By combining Eqs. (I-1)-(I-3), we get

$$f = \frac{\bar{\alpha}_Q d/H}{\bar{\alpha}_Q \frac{d}{H} + \alpha_{\text{InP}} + \frac{0.042(L+W)}{LW}} \quad (I-4)$$

The magnitude of  $f$  will be of great importance in the laser characteristics. Using Eq. (I-4), we have evaluated  $f$  as a function of active layer thickness  $d$  for typical device dimensions and several possible values of  $\alpha_{\text{InP}}$  and  $\bar{\alpha}_Q$ . The results are shown in Fig. 1-5.

Fig. 1-5. The fraction of spontaneous photons reabsorbed by the GaInAsP active layer in the broad-area GaInAsP/InP DH laser (Fig. 1-4), obtained by the present calculation [Eq. (I-4)].



The immediate effect of the reabsorption of the spontaneous photons is an effective lengthening of the radiative carrier lifetime and the consequent lowering of the laser threshold current density. To see this, we suppose that the radiative carrier lifetime without the reabsorption is  $\tau_r$ . With the reabsorption, the effective radiative carrier lifetime is now

$$\tau_r = \frac{\tau_r}{1-f} \quad (1-5)$$

The ratio of the threshold current densities with and without the reabsorption is then given by

$$\frac{J_{th}' \text{ (with reabsorption)}}{J_{th} \text{ (without reabsorption)}} = \frac{\tau}{\tau'} \quad (1-6)$$

where  $\tau' \equiv \tau_{nr} \tau_r' / \tau_{nr} + \tau_r'$  and  $\tau \equiv \tau_{nr} \tau_r / \tau_{nr} + \tau_r$  are total carrier lifetimes with and without the reabsorption, respectively. ( $\tau_{nr}$  is the nonradiative carrier lifetime.) After some rearranging, the lowering of the threshold current density can be expressed as

$$\frac{J_{th} - J_{th}'}{J_{th}} = \eta f \quad (1-7)$$

where  $\eta \equiv \tau_{nr} / (\tau_{nr} + \tau_r)$  is the internal quantum efficiency of the laser without the reabsorption. Note that  $\eta$  will be a limiting factor in the threshold-current lowering.

In Eq.(1-3) an average absorption coefficient  $\bar{\alpha}_Q$  has been used for the band-to-band reabsorption of the spontaneous photons. The value of  $\bar{\alpha}_Q$  will depend on the functional dependence of the absorption coefficient on energy, which in turn depends on the band structure and electron-hole injection.<sup>14</sup> Those spontaneous photons with energies in the gain region (the lower energy portion of the spontaneous spectrum)<sup>15</sup> will have a net probability of being amplified, rather than being absorbed, when passing through the active layer. These photons will not only make a negative contribution to  $f$  but probably will also contribute to the noise in the laser emission. However, with gain  $\leq 100 \text{ cm}^{-1}$  these photons will more likely be absorbed in the InP or be transmitted through the device sidewalls.

The present calculations show that for the general case of broad-area GaInAsP/InP lasers, appreciable amounts of reabsorption of the spontaneous photons and lowering of the laser threshold current density can occur [Fig. 1-5 and Eq. (1-7)]. Based on the same calculations, improved results can be expected if the device structure is optimized to minimize the free-carrier absorption in InP and the transmission loss through the sidewalls and/or to enhance the absorption in the active layer. These can be achieved by using low substrate doping, a thin substrate, Au-coated sidewalls (except for the laser emission region), and a thicker active layer, etc. In addition to the broad-area lasers, the same concept can be applied to other laser structures. Among the stripe-geometry lasers, the buried-heterostructure and strip-buried heterostructure lasers are most pertinent, because there is no unpumped region of the GaInAsP layer which will contribute to the loss of spontaneous light. The same principles can also be applied to the GaAs/GaAlAs lasers if the highly absorbing GaAs substrates can be removed or optically isolated from the finished devices.

The reabsorption of the spontaneous photons is also likely to affect the temperature dependence of the threshold current. Generally speaking, the increase of threshold current accompanying an increase in temperature is mainly due to an increase in the energy spread of the injected carriers. The result is that the maximum gain is lowered and more carriers are wasted

in generating spontaneous emission.<sup>14</sup> This will also cause an increase in  $\bar{\alpha}_Q$  and a consequent increase in  $f$ . Reabsorption of spontaneous photons will thus have a tendency to reduce the temperature dependence of the threshold current and to increase the reliability of the device.

Z. L. Liao  
J. N. Walpole

### C. HIGH-PERFORMANCE ELEVATED-TEMPERATURE PHOTOMIXERS FOR CO<sub>2</sub> LASER SYSTEMS

P-type HgCdTe photoconductors have been investigated for use as photomixers at temperatures above 77 K in tactical CO<sub>2</sub> laser systems demanding the simplicity and reliability of a thermoelectrically cooled detector. The physics of heterodyne operation of intrinsic photoconductors has been examined, and numerous specially designed p-type HgCdTe photoconductors have been fabricated and evaluated. These 100- $\mu$ m-square devices have shown heterodyne sensitivities at 38 MHz of  $5 \times 10^{-20}$  W/Hz at 77 K and  $1.8 \times 10^{-19}$  W/Hz at 195 K, with bandwidths of 140 and 30 MHz, respectively. Bandwidths in excess of 100 MHz at 195 K have been obtained with sensitivities of about  $4 \times 10^{-19}$  W/Hz.

At low temperatures, photodiodes, which have shown noise equivalent powers (NEPs) as low as  $3 \times 10^{-20}$  W/Hz, are fundamentally better CO<sub>2</sub> laser photomixers than photoconductors.<sup>16,17,18</sup> However, as the detector temperature is increased above about 160 K, 10- $\mu$ m photoconductors will begin to outperform photodiodes. In order to obtain quantum-noise-limited operation, the CO<sub>2</sub> laser local oscillator power absorbed by the photoconductor must be such that (1) the density of photogenerated carriers exceeds the background minority carrier density and (2) the generation-recombination noise associated with the photocarriers exceeds the Johnson or thermal noise ( $4kT/R$ ) of the photoconductor. The first condition above is equivalent to the photodiode requirement that the photocurrent exceed the thermally generated dark current. The local oscillator powers needed to satisfy these requirements for the photoconductor and photodiode are virtually identical, with the same temperature dependence. The advantage photoconductors have over photodiodes comes from condition (2) above, i.e., overcoming Johnson noise. At high temperatures the junction resistance of 0.12-eV photodiodes goes to zero, whereas relatively high resistance can be obtained with a p-type HgCdTe photoconductor because of the low mobility of holes.

The bandwidth of a photoconductor is determined by the lifetime of the minority carriers, which in small-energy-gap p-type HgCdTe is controlled by Auger recombination processes and is a strong function of carrier concentration. The dashed curve in Fig. I-6 shows the calculated Auger-limited bandwidth of p-type, 10- $\mu$ m HgCdTe photoconductors at 200 K as a function of hole concentration.<sup>19</sup> Data we have accumulated on the pulse response of many different devices are consistent with this curve. The solid curves in Fig. I-6 are the calculated local oscillator powers required to satisfy the two conditions above, i.e., photogenerated electron concentration equal to background electron concentration and g-r noise equal to thermal noise. A minority electron mobility of 10,000 cm<sup>2</sup>/V-sec was assumed as well as unit quantum efficiency ( $\eta = 1$ ). The power required to overcome thermal noise varies as  $V^{-2}$ , but Joule heating places a practical limit to the bias voltage. One volt was used for this calculation. A minimum in the calculated LO power occurs for  $p = 3 \times 10^{16}$  cm<sup>-3</sup> (about 3 times the intrinsic carrier concentration), with a corresponding bandwidth of 12 MHz. For a 100-MHz bandwidth, a laser power of about 10 mW is calculated for LO-noise-limited operation. LO-noise-limited operation at 1 GHz

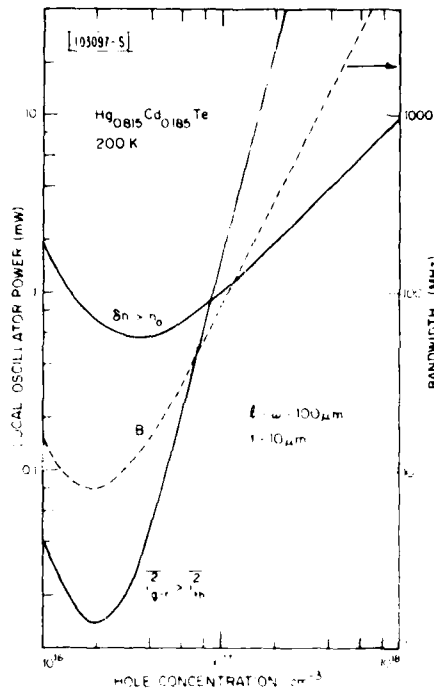


Fig. 1-6. Calculated bandwidth and heterodyne LO power requirements at 200 K as a function of hole concentration for p-type HgCdTe photoconductors.

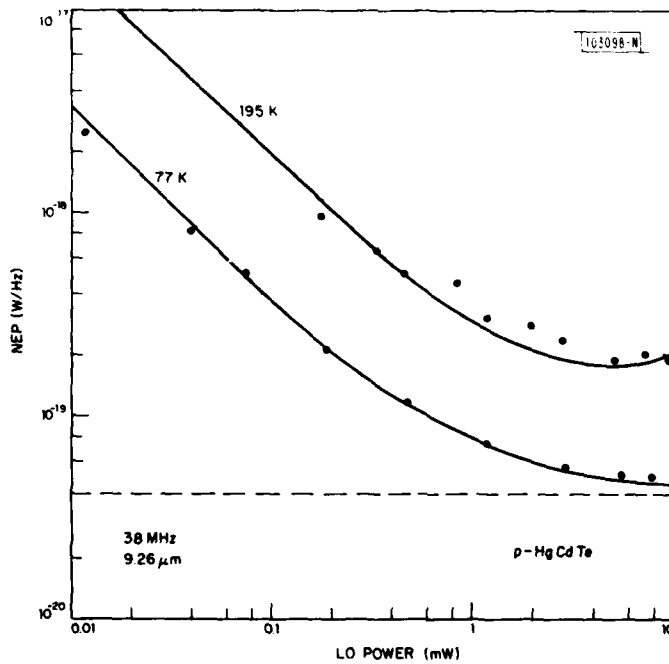


Fig. 1-7. Measured and calculated NEP as a function of LO power for a p-type HgCdTe photoconductor at 77 and 195 K.

appears beyond possibility due to the over 100 mW requirement in these small area ( $100 \mu\text{m} \times 100 \mu\text{m}$ ) devices and the associated heating.

Many different p-type photoconductors were fabricated by epoxy-bonding p-type HgCdTe to sapphire substrates and thinning to about  $10 \mu\text{m}$ . Acceptor concentrations ranged from about  $2 \times 10^{17} \text{cm}^{-3}$  to less than  $1 \times 10^{16} \text{cm}^{-3}$ , and energy gaps at 200 K ranged from 0.14 to about 0.11 eV. Bandwidths in excess of 500 MHz were observed for the high acceptor concentrations, but the photoconductance was small (typically of the order of 0.1 m mho/mW at  $10.6 \mu\text{m}$ ) due principally to the short lifetimes. Quantum efficiency, lifetime and minority electron mobility were determined on many of these devices by analyzing the results of responsivity, pulse response, and heterodyne sensitivity measurements. Minority electron mobility values ranged from about 3,000 to about  $10,000 \text{cm}^2/\text{V-sec}$  and did not appear to change from 77 to 195 K.

Two techniques were used to measure heterodyne NEP: blackbody heterodyne radiometry and the mixing of two coherent  $\text{CO}_2$  beams offset by 38 MHz with an acoustooptic modulator. Results from the two methods were in good agreement. Although the acoustooptic modulator technique was limited to a single beat frequency, much higher sensitivity was achieved. In Fig. I-7, the NEP as a function of local oscillator power is shown for a detector at 77 and 195 K. At 77 K this device shows a heterodyne sensitivity very close to that of an ideal photoconductor (indicated by the dashed line in Fig. I-7). The g-r noise of the local oscillator equaled the total noise from all other sources (primarily Johnson noise) at a power level of only 0.7 mW. The solid curve going through the 77 K data was calculated from the simple asymptotic expression,

$$\text{NEP} = (2h\nu B/\eta) (1 + P_o/P_{LO})$$

where B is the noise bandwidth,  $\eta$  is the quantum efficiency, and  $P_o$  is the equivalent background noise power (0.7 mW).

At 195 K the minimum NEP is about 4 times higher than at 77 K. This loss in sensitivity is due to a combination of lower quantum efficiency (~50%) and higher background noise ( $P_o \sim 2 \text{mW}$ ). In addition, at 195 K both  $\eta$  and  $P_o$  are strong functions of temperature and heating is an important consideration. The energy gap of HgCdTe increases with increasing temperature, resulting in a decrease in absorption coefficient and  $\eta$ . Also  $P_o$  is a very strong function of the intrinsic carrier concentration, which increases exponentially with temperature.<sup>20</sup> Consequently, heating due to the local oscillator causes  $\eta$  to decrease and  $P_o$  to increase, resulting in a minimum in the NEP-vs- $P_{LO}$  curve. The 195 K curve in Fig. I-7 was calculated assuming a heating factor of 1 K/mW, which is consistent with calculated and measured values. The minimum NEP of  $1.8 \times 10^{-19} \text{W/Hz}$  is the best value reported to date for a  $\text{CO}_2$  laser photomixer at 195 K. Pulse response measurements indicated that this device had a 3-dB rolloff frequency of 140 MHz at 77 K and 30 MHz at 195 K. The magnitude and temperature dependence of the bandwidth are in agreement with the calculated Auger recombination times<sup>19</sup> for HgCdTe with  $p = 5 \times 10^{16} \text{cm}^{-3}$ . Bandwidths of over 100 MHz have been obtained with a NEP in the vicinity of  $4 \times 10^{-19} \text{W/Hz}$  at 195 K.

With further optimization of the photoconductor structure, including better heat sinking, we calculate that a NEP of  $1 \times 10^{-19} \text{W/Hz}$  and a bandwidth of 150 MHz could be obtained at 250 K. A room-temperature  $\text{CO}_2$  laser photomixer with a NEP of  $3 \times 10^{-19} \text{W/Hz}$  and a bandwidth of 200 MHz should also be realized with p-type HgCdTe photoconductors.

D. L. Spears  
P. E. Duffy  
C. D. Hoyt

## REFERENCES

1. Solid State Research Report, Lincoln Laboratory, M.I.T. (1979:4), p. 9, DDC AD-A084271.
2. DuPont polyimide PI-2555.
3. S. R. Chinn and W. K. Zwicker, *Appl. Phys. Lett.* 34, 847 (1979); also Solid State Research Report, Lincoln Laboratory, M.I.T. (1979:1), p. 25, DDC AD-A073152/1.
4. K. Nishida, K. Taguchi, and Y. Matsumoto, *Appl. Phys. Lett.* 35, 251 (1979).
5. K. Taguchi, Y. Matsumoto, and K. Nishida, *Electron. Lett.* 15, 453 (1979).
6. H. Melchior and W. T. Lynch, *IEEE Trans. Electron. Devices* ED-13, 829 (1966).
7. S. R. Forrest, M. DiDomenico, Jr., R. G. Smith, and H. J. Stocker, *Appl. Phys. Lett.* 36, 580 (1980).
8. G. E. Stillman and C. M. Wolfe, "Avalanche Photodiodes," in Semiconductors and Semimetals, Vol. 12, R. K. Willardson and A. C. Beer, Eds. (Academic Press, New York, 1977), p. 365.
9. R. J. McIntyre, *IEEE Trans. Electron. Devices* ED-13, 154 (1966).
10. R. J. McIntyre, *IEEE Trans. Electron. Devices* ED-19, 703 (1972).
11. C. A. Armiento, S. H. Groves, and C. E. Hurwitz, *Appl. Phys. Lett.* 35, 333 (1979).
12. M. Ito, T. Kaneda, K. Nakajima, Y. Toyoma, and T. Kotani, *Electron. Lett.* 14, 418 (1978).
13. H. Kressel and J. K. Butler, Semiconductor Lasers and Hetero-junction LEDs (Academic Press, New York, 1977), p. 135.
14. H. C. Casey, Jr. and M. B. Panish, Heterostructure Lasers, Parts A and B (Academic Press, New York, 1978).
15. See, for example, Ref. 1, p. 110.
16. D. L. Spears, *Infrared Physics* 17, 5 (1977).
17. Solid State Research Report, Lincoln Laboratory, M.I.T. (1978:3), p. 1, DDC AD-A065116/6.
18. D. L. Spears, *Proc. SPIE*, Vol. 227 (to be published).
19. T. M. Casselman and P. F. Peterson, *Solid State Commun.* 33, 615 (1980).
20. Y. Nemirovsky and F. Finkman, *J. Appl. Phys.* 50, 8197 (1979).

## II. QUANTUM ELECTRONICS

### A. Q-SWITCHING AND MODE-LOCKING OF TRANSITION METAL LASERS

Tunable, Q-switched operation has been observed in Ni:MgF<sub>2</sub> and Co:MgF<sub>2</sub> lasers under CW pumping conditions. A Ni:MgF<sub>2</sub> laser, operating at 1.67 μm, has been mode-locked to produce ~100-psec-wide pulses at a 247-MHz repetition rate.

Previous Q-switching results<sup>1</sup> were limited by the static and dynamic losses introduced by the LiNbO<sub>3</sub> electrooptic Q-switch used. The data presented here were obtained with a Brewster-angle, fused-silica acoustooptic Q-switch, which had a negligible insertion loss. The laser system was a 3-mirror design described previously<sup>2</sup> and employed a 1.2-cm-long, Brewster-angle laser crystal, cooled to ~80 K and pumped by a 2-W, TEM<sub>00</sub>-output, 1.33-μm Nd:YAG laser.

The peak and average power outputs vs repetition rate for Ni:MgF<sub>2</sub> and Co:MgF<sub>2</sub> are shown in Figs. II-1 and II-2, respectively. The pulsewidth of the Ni:MgF<sub>2</sub> laser varied from 0.7 μsec at low repetition rates to 3.5 μsec at 2 kHz, while that of the Co:MgF<sub>2</sub> laser varied from 1.0 μsec at 100 Hz to 5.0 μsec at 5 kHz. At high repetition rates for both systems, the average power output was essentially the same as the CW output. For Ni:MgF<sub>2</sub> the extracted energy density was ~2.5 J/cm<sup>3</sup>.

Tunable Q-switched operation was observed from Ni:MgF<sub>2</sub> and Co:MgF<sub>2</sub> lasers by insertion of a single-element birefringent filter in the laser cavity. Figure II-3 presents the peak power output at a pulse rate of 100 Hz as well as the CW output vs wavelength for Ni:MgF<sub>2</sub>. Data on tunable Q-switching of the Co:MgF<sub>2</sub> laser have not yet been taken over the full CW tuning range (from 1.63 to 2.11 μm), but Q-switched output was obtained from 1.64 to 1.89 μm.

The rolloff in peak power for Ni:MgF<sub>2</sub> at repetition rates >200 Hz is not in accord with standard theory<sup>3</sup> for CW-pumped, repetitively Q-switched lasers, which predicts a rolloff around 80 Hz, the inverse of the 12-msec Ni:MgF<sub>2</sub> upper-state lifetime. The Nd:YAG pump-laser intensity is sufficiently intense to partially saturate the Ni<sup>2+</sup> transition in absorption, however, and such saturation may explain the discrepancy. The power vs rate behavior of the Co:MgF<sub>2</sub> laser is in good agreement with theory, given the 1.3-msec lifetime of that system. In Q-switched operation, the pulse output energy increases linearly with pump power while the pulse width decreases. Thus, compared with CW output power, Q-switched peak-power output is a more sensitive function of the ratio of pump power to threshold pump power. Since this ratio changes as the laser is tuned at constant pump power, the wider variation with wavelength in power output for peak power than for CW power is expected in the tuning results of Fig. II-3.

The large gain-bandwidth of the Ni:MgF<sub>2</sub> and Co:MgF<sub>2</sub> lasers should allow generation of picosecond pulses under mode-locked conditions. A preliminary experiment in mode-locking was carried out on the three-mirror-cavity Ni:MgF<sub>2</sub> laser. An intracavity electrooptic loss modulator consisting of a 2-cm-long, Brewster-angle-cut crystal of LiNbO<sub>3</sub> was used for active mode-locking. The modulator was driven by 5 W of RF power through an LC impedance-matching network at a frequency of ~123.4 MHz, half the round-trip frequency of the laser cavity. The peak loss was estimated to be about 5 percent. Extremely careful adjustment of both pump beam alignment and RF drive frequency was required to obtain a mode-locked output free of relaxation oscillations; tolerance on the drive frequency was less than 1 kHz. The 10-mW, 1.67-μm output, as detected by a Ge avalanche photodiode and viewed on a sampling oscilloscope, is shown in Fig. II-4. The pulsewidth indicated is undoubtedly detector limited. The frequency spectrum of

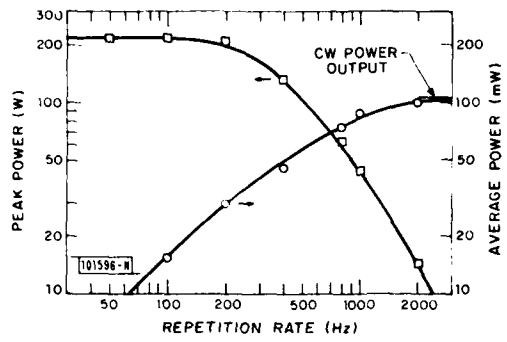


Fig. II-1. Peak pulse power and average power from a Q-switched Ni:MgF<sub>2</sub> laser.

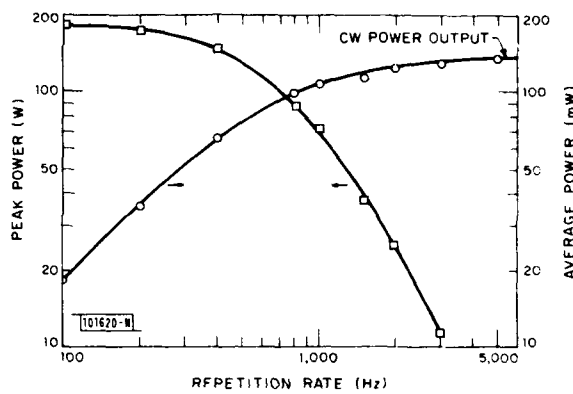


Fig. II-2. Same as Fig. II-1 except for Co:MgF<sub>2</sub> laser.

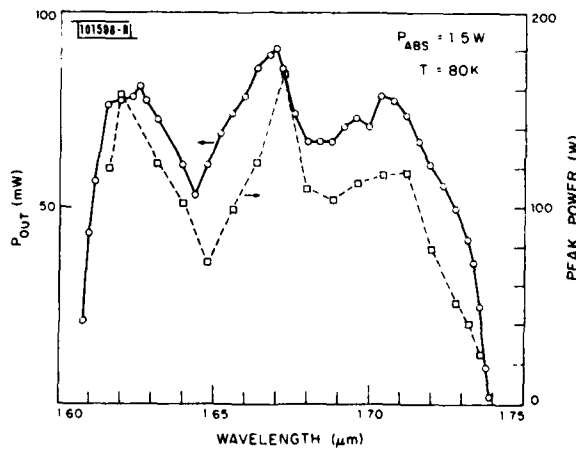
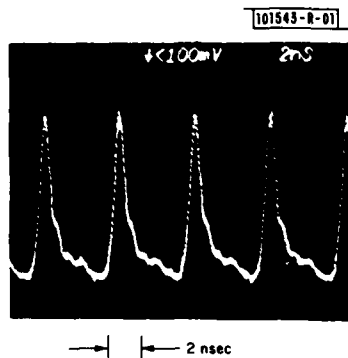


Fig. II-3. Tuning curves for Q-switched and CW Ni:MgF<sub>2</sub> lasers.

Fig. II-4. Mode-locked pulses from Ni:MgF<sub>2</sub> laser.



the laser, as determined by a scanning confocal interferometer with a free-spectral-range (FSR) of 7.5 GHz appears in Fig. II-5. A higher resolution view of Fig. II-6 shows at least three overlapping orders of modes, i.e., the FSR is too small to properly view the mode spectrum. What is evident from Fig. II-5, however, is a deep modulation of the mode spectral envelope, caused by some etalon or etalon-like effect in the laser cavity, which produces at least three clusters of modes. Without the deep modulation, the approximate pulsewidth predicted<sup>4</sup> from the unfolded 15-GHz FWHM linewidth of the mode spectrum would be  $\sim 30$  psec. The modulation broadens the temporal width of the main pulse and would also generate weak satellite pulses spaced  $\sim 130$  psec on either side of the main pulse, providing that phase coherence is maintained among the clusters.<sup>5</sup>

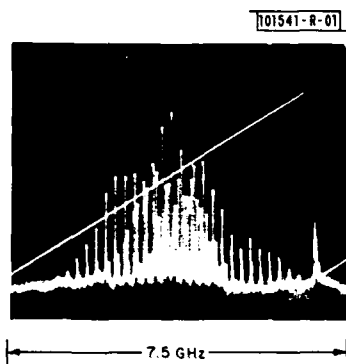


Fig. II-5. Scanning-interferometer spectrum from mode-locked Ni:MgF<sub>2</sub> laser.

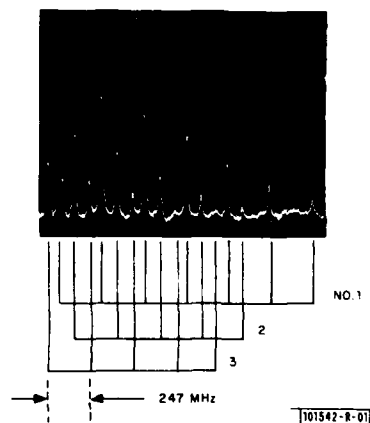


Fig. II-6. Expanded scan of Fig. II-5, showing three clusters of modes.

It is expected that use of an improved loss modulator, such as an acousto-optic cell similar to that used for Q-switching, and elimination of the presently unexplained etalon effect in the laser cavity would both increase the power output and decrease the pulsewidth of the mode-locked Ni:MgF<sub>2</sub> laser.

P. F. Moulton  
A. Mooradian

## B. SEMICONDUCTOR OPTICAL NONLINEARITIES

There has recently been increased interest in the use of nonlinear optical effects in semiconductor materials for bistable switch operation<sup>6,7</sup> and for optical phase conjugation.<sup>8,9</sup> Much of the bistability work has been motivated by the potential use of such devices in optical signal processing applications. Although the interest in phase conjugation stems from a different area, the same nonlinear mechanisms contribute to both effects.

Bistability results when a medium with an intensity-dependent refractive index is placed within a Fabry-Perot optical cavity. The resonator structure provides the optical feedback necessary for the bistable operation. This configuration is shown in Fig. II-7(a). It is also possible to visualize integrated circuit analogs of this device such as shown in Fig. II-7(b). A hybrid three-port switch which uses an external laser source to control the transmission of an integrated optical structure is shown schematically in Fig. II-7(c). There has also been a recent report<sup>10</sup> of bistability associated with reflection at a nonlinear medium boundary for incident angles close to the critical angle. This is closely related to optical propagation in semiconductor waveguides and should lead to additional types of integrated optical bistable devices.

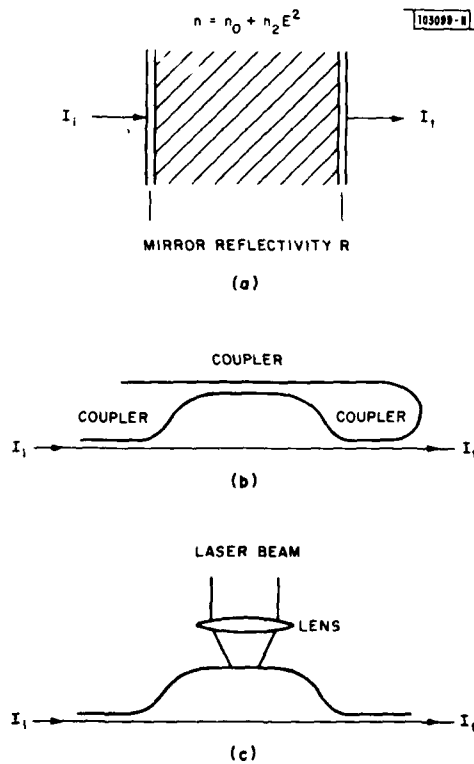


Fig. II-7. Bistable optical devices: (a) Fabry-Perot resonator filled with a nonlinear optical material, (b) integrated optical analog of (a), (c) three-port integrated optical device.

A variety of mechanisms give rise to the nonlinear dielectric response of a semiconductor. Intrinsic properties include:

- (1) Valence electronic backgrounds,
- (2) Carrier nonparabolicity effects,

- (3) Optical carrier generation effects, and
- (4) Optical redistribution of mobile carriers.

The first two processes do not involve changing the distribution of carriers in the semiconductor and thus respond at all frequencies up to optical transition frequencies of  $10^{14}$  to  $10^{15}$  Hz. Processes (3) and (4) involve carrier redistribution and are therefore limited by the relaxation of these carriers back to their equilibrium distributions. This time scale may vary from  $\sim 10^{-11}$  sec for electron LO phonon relaxation to  $\sim 10^{-7}$  sec for radiative recombination in narrow-gap semiconductors. Another major advantage of the first two processes is that they do not involve, to first order, any optical absorption and hence any energy deposition in the semiconductor. Carrier redistribution processes, in contrast, depend on optical absorption and, if they are to be sufficiently fast, on the carriers giving up that energy to the lattice with consequent heating problems.

#### 1. Valence Electronic Background

Here we consider the contribution from an intrinsic semiconductor at  $T = 0$ , i.e., a filled valence band and an empty conduction band. Jha and Bloembergen<sup>11</sup> have calculated the third-order susceptibilities for a number of common semiconductors. Their results, which are approximate and do not treat the effects of resonance enhancement for near-bandgap radiation, are reproduced in Table I. Since contributions from the entire Brillouin zone are included,

TABLE I CALCULATED VALENCE BAND CONTRIBUTIONS TO $n_2$ (After Jha and Bloembergen <sup>6</sup> )	
	$n_2 = (2\pi/n_0) \times \overset{(3)}{\underset{1111}{\chi}} \text{ (esu)}$
Ge	$-5.5 \times 10^{-10}$
Si	$-5.0 \times 10^{-11}$
InSb	$-8.0 \times 10^{-9}$
GaAs	$-1.0 \times 10^{-10}$

resonance effects should be less important for the valence band susceptibility than for the zone-center free-carrier contributions to the third-order susceptibility discussed below. The notation used in the table and throughout the text follows the usual convention:

$$n = n_0 + n_2 E^2 \tag{II-1}$$

where the electric field is given by  $E = \epsilon(e^{i\omega t} + e^{-i\omega t})$ .

#### 2. Carrier Nonparabolicity

Because of the nonparabolic band structure of III-V compounds, mobile carriers respond anharmonically to harmonic driving forces and thus present a nonlinear susceptibility. In addition

to this effect, optical absorption by mobile carriers changes their linear susceptibility and thus represents a nonlinear response; this is discussed in Section 4. For the present, these separate analyses may be used to estimate the importance of various effects. A detailed theory which includes all of the effects simultaneously will ultimately be required. Patel *et al.*,<sup>12</sup> first measured the free-carrier contribution to the susceptibility by frequency mixing experiments between two CO<sub>2</sub> lasers. They found  $n_2$ 's of  $4 \times 10^{-9}$  esu (InSb;  $N_e = 6 \times 10^{16}$  cm<sup>-3</sup>) and  $4 \times 10^{-11}$  esu (GaAs;  $N_e = 1.5 \times 10^{16}$  cm<sup>-3</sup>).

The nonlinear susceptibility for this process may be evaluated using the general expressions given in Ref. 13. The calculation involves three virtual interband transitions, and the  $n_2$  is highly resonant for near bandgap radiation. The result is

$$n_2 = \left( \frac{2\pi N_e e^4}{n_0 m_e^2 \epsilon_g \omega^4} \right) \left( \frac{\epsilon_g^4 [\epsilon_g^2 + (\hbar\omega)^2/3]}{[\epsilon_g^2 - (\hbar\omega)^2]^3} \right). \quad (\text{II-2})$$

This equation has been written as the product of the single-band-model  $n_2$  (Ref. 14) and a resonance enhancement factor, which is only applicable for  $\epsilon_F \ll \epsilon_g - \hbar\omega$ . More detailed calculations are necessary for higher concentrations or nearer resonance conditions.

### 3. Optical Carrier Generation Effects

Carriers generated by near bandgap radiation modify both the real and imaginary parts of the dielectric response. A  $k \cdot p$  model calculation of the real part of the linear susceptibility for an input frequency below a III-V semiconductor direct gap  $\epsilon_g$  has been carried out. For a Fermi energy  $\epsilon_F \ll \epsilon_g - \hbar\omega$ , the result is

$$\Delta n = - \frac{2\pi N_e e^2}{n_0 m_e \omega^2} \frac{\epsilon_g^2}{\epsilon_g^2 - (\hbar\omega)^2}. \quad (\text{II-3})$$

The generated carrier concentration  $N_e$  is given by the rate equation

$$\frac{dN_e}{dt} = - \frac{N_e}{\tau_r} + \frac{\alpha I}{\hbar\omega} \quad (\text{II-4})$$

where  $\tau_r$  is the carrier recombination time,  $\alpha$  the absorption constant (due to impurity levels and band tailing), and  $I$  the light intensity. For times long compared with  $\tau_r$ , the steady-state solution to Eq. (II-4) may be used in (II-3); the result for the nonlinear index of refraction, again for  $\epsilon_F \ll \epsilon_g - \hbar\omega$ , is

$$n_2 = - \frac{\alpha e^2 \tau_r c}{4\hbar\omega^3 m_e} \frac{\epsilon_g^2}{\epsilon_g^2 - (\hbar\omega)^2} \quad (\text{II-5})$$

### 4. Carrier Redistribution Effects

Similar effects result when existing carriers are redistributed within the conduction or valence bands by free-carrier absorption processes. Far from resonance, the free-carrier

contribution to the semiconductor dielectric response is

$$n^2 = n_0^2 - \sum_i \frac{4\pi N_i e^2}{m_i \omega^2} \quad (\text{II-6})$$

where the summation runs over the conduction and valence bands. Resonance effects enhance this contribution for  $\hbar\omega \lesssim \epsilon_g$ . For n-type material, conduction band nonparabolicity and intervalley transitions are mechanisms which give an energy-dependent effective mass. For p-type III-V compounds, heavy-to-light hole transitions provide a potential nonlinearity. While the detailed kinetics are not well known for all of these processes, they are thought to relax on the electron-LO phonon scattering time scale of 1 to 10 psec. The calculations are similar to those given in Section 3 and only results are quoted here: for light-hole-heavy-hole transitions

$$n_2 = -\frac{e^2 \alpha \tau c}{4\hbar\omega^3} \frac{\epsilon_g^2}{\epsilon_g^2 - (\hbar\omega)^2} \left( \frac{1}{m_l} - \frac{1}{m_h} \right) \quad (\text{II-7})$$

for conduction electron nonparabolicity

$$n_2 = \frac{e^2 \alpha \tau c}{8m_e \epsilon_g \omega^2} \frac{\epsilon_g^2}{\epsilon_g^2 - (\hbar\omega)^2} \quad (\text{II-8})$$

and for intervalley transitions

$$n_2 = \frac{e^2 \alpha \tau c}{4\hbar\omega^3} \left( \frac{1}{m_e} \frac{\epsilon_g^2}{\epsilon_g^2 - (\hbar\omega)^2} - \frac{1}{m_v} \right) \quad (\text{II-9})$$

The carrier generation process for GaAs (and for InP) is limited by recombination processes to switching speeds of  $\sim 1$  nsec. This speed may be enhanced, with a proportionate decrease in  $n_2$ , by doping with deep-level impurities or by surface recombination processes. In this case the limiting intensity is set by damage thresholds and is typically  $10^8$  W/cm<sup>2</sup> for 100-nsec pulses and will be even higher for short pulses. Thus, switches at about 1  $\mu\text{m}$  using carrier generation in GaAs or InP with switching speeds of 50 to 100 psec appear feasible. For devices which employ the nonparabolicity mechanism, multiphoton absorption sets an intensity limitation of approximately  $10^6$  W/cm<sup>2</sup>.

Table II presents a compilation of the results of these calculations. A resonance enhancement of 10 for the linear susceptibilities and of  $10^3$  for the third-order susceptibility was used in the calculation.

The results presented here are preliminary, idealized calculations. Effects such as carrier generation and carrier heating both occur at the same time and tend to cancel each other. Further calculations and experiments are necessary to fully evaluate these nonlinear processes.

S. R. J. Brueck

### C. FIELD OPERATION OF A SUBMILLIMETER HETERODYNE RADIOMETER

A number of modifications made on the quasi-optical corner reflector mixer have resulted in an improvement of about a factor of 3 in the system noise temperature. With a specially designed network matching the diode to the IF circuit and a low-noise FET amplifier, the best

TABLE II  
CALCULATED NONLINEAR COEFFICIENTS

Mechanism	Material	Material Limiting Speed (psec)	$ n_2 $ (esu)	
Valence Background	GaAs	<0.001	$1.0 \times 10^{-10}$	
	InSb	<0.001	$8.0 \times 10^{-9}$	
Conduction Electron Nonparabolicity	GaAs ( $N_e = 1 \times 10^{16}$ )	<0.001	$1.0 \times 10^{-11}$	
	InSb ( $N_e = 1 \times 10^{16}$ )	<0.001	$9.0 \times 10^{-7}$	
Carrier Generation	GaAs	1,000	$4.0 \times 10^{-8}$	
	InSb	10,000	$4.0 \times 10^{-4}$	
Carrier Heating	(a) intervalley	GaAs	10	$2.0 \times 10^{-10}$
		GaAs	10	$1.0 \times 10^{-10}$
	(b) nonparabolicity	InSb	10	$1.5 \times 10^{-7}$
		GaAs	10	$1.0 \times 10^{-10}$
	(c) hole transitions	GaAs	10	$1.0 \times 10^{-10}$
		InSb	10	$3.0 \times 10^{-7}$

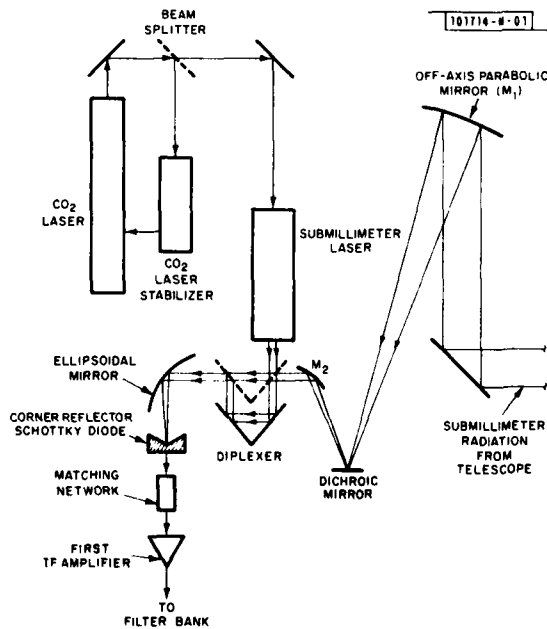


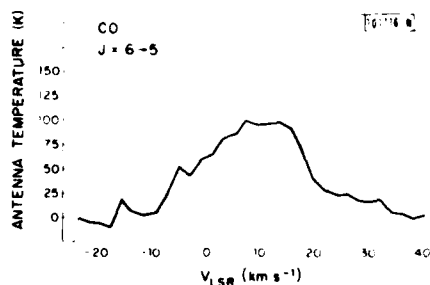
Fig. II-8. The experimental setup includes a specially stabilized optically pumped submillimeter laser, a quasi-optical mirror system to couple radiation from the telescope, and the radiometer with associated electronics.

system noise temperature  $T_S$  measured at 433  $\mu\text{m}$  was 2900 K (DSB). The mixer noise temperature  $T_M$  is 2300 K, and the DSB conversion loss  $L_C$  is 9.4 dB.

The radiometer/receiver was developed for possible short-range submillimeter radar imaging, remote sensing of atmospheric constituents, and plasma diagnostics. After initial laboratory simulation experiments, the system was also considered for radiometric space surveillance of missile plumes. Now, with the improvement in system noise temperature by a factor of 3, the required integration time for a given signal to noise in our radiometric measurements has been reduced by a factor of 9. This has made ground-based, high-resolution submillimeter radio astronomy possible with reasonable integration times. Consequently, a field experiment was undertaken involving the detection of molecular emission from interstellar clouds.

The radiometer was used with NSF support and in collaboration with NASA/Goddard and the Five College Radio Observatory, University of Massachusetts, Amherst, at the 3.0 m NASA Infrared Telescope Facility on 14,000-ft Mauna Kea, Hawaii. Measurements of CO in the molecular cloud Orion at 694 GHz were carried out using an optically pumped far-IR laser local oscillator. Emission at these wavelengths could also be observed from Venus and the sun, thereby demonstrating the feasibility of future measurements of planetary atmospheric constituents. Figure II-8 shows the experimental setup, and Fig. II-9 shows the  $J = 6 \rightarrow 5$  spectral line of CO in Orion. The intensity (i.e., the corrected radiometric temperature) of this transition when compared with the previously measured  $J = 3 \rightarrow 2$  emission, supports the interpretation that the broad CO feature is optically thin ( $\tau < 0.5$ ) and that it is produced in a hot region whose excitation temperature is greater than 180 K.

Fig. II-9. The trace of CO emission from Orion shows a full width at half maximum of  $26 \text{ km s}^{-1}$ . The ordinate is antenna temperature corrected for atmospheric extinction and a forward beam coupling efficiency of 0.36.



These initial observations demonstrate that the submillimeter radiometer system can be successfully fielded and opens up the new area of high-resolution ground-based submillimeter astronomy. A more complete description of the instrumentation, observations and results will appear elsewhere.<sup>15</sup>

H. R. Fetterman    D. D. Peck  
B. J. Clifton      P. E. Tannenwald

\*G. A. Koepf, D. Buhl, and N. McAvoy, NASA/Goddard; P. F. Goldsmith and N. R. Erickson, University of Massachusetts.

#### REFERENCES

1. Solid State Research Report, Lincoln Laboratory, M.I.T. (1978:4), p. 18, DDC AD-A068563/6.
2. Solid State Research Report, Lincoln Laboratory, M.I.T. (1978:3), p. 7, DDC AD-A065116/6.
3. R. B. Chesler, M. A. Karr, and J. E. Geusic, Proc. IEEE 58, 1899 (1970).
4. D. J. Kuizenga and A. E. Siegman, IEEE J. Quantum Electron. QE-6, 694 (1970).
5. S. R. Chinn, Opt. Commun. 31, 359 (1979).
6. H. M. Gibbs, S. L. McCall, T. N. C. Venkatesan, A. C. Grossard, A. Passner, and W. Wiegman, Appl. Phys. Lett. 35, 451 (1979).
7. D. A. B. Miller, S. D. Smith, and A. Johnston, Appl. Phys. Lett. 35, 658 (1979).
8. J. F. Ready, M. A. Khan, and P. W. Kruse, Paper presented at 1979 Annual Meeting of Optical Society of America.
9. R. K. Jain and M. B. Klein, Appl. Phys. Lett. 35, 454 (1979).
10. P. W. Smith, J.-P. Hermann, W. J. Tomlinson, and P. J. Maloney, Appl. Phys. Lett. 35, 846 (1979).
11. S. S. Jha and N. Bloembergen, Phys. Rev. 171, 891 (1968).
12. C. K. N. Patel, R. E. Slusher, and P. A. Fleury, Phys. Rev. Lett. 17, 1011 (1966).
13. P. N. Butcher and T. P. McLean, Proc. Phys. Soc. 81, 219 (1963).
14. P. A. Wolff and G. A. Pearson, Phys. Rev. Lett. 17, 1015 (1966).
15. Submitted to Science and Astrophysical Journal.

### III. MATERIALS RESEARCH

#### A. CRYSTAL GROWTH OF InP BY THE LEC TECHNIQUE

We have been using the liquid-encapsulated Czochralski (LEC) technique for the growth of InP single crystals needed to supply substrates for research on optoelectronic devices. Boules of InP grown by this technique have a strong tendency to twin, due to the very low stacking fault energy of InP (Ref. 1). Since twinning is generally followed by polycrystalline growth, the yield of useful crystals will be extremely small unless twinning can be prevented. We have therefore developed a standard growth procedure that minimizes the probability of twinning but does not result in excessive dislocation densities. For most impurity dopants, this procedure gives a high yield of boules that are twin-free over most of their length.

The LEC growth is carried out in a high-pressure crystal puller with water-cooled walls. A diagram of the assembly used for our standard growth procedure is shown in Fig. III-1. The seed is a (111)-oriented crystal that is mounted with the P face down on a BN holder attached to a water-cooled pulling rod. A pyrolytic BN crucible is loaded with a charge of polycrystalline InP weighing 300 g, the desired weight of dopant (if any), and a charge of  $B_2O_3$  encapsulant that is pre-baked in vacuum to reduce its water content. The crucible is placed in a high-purity graphite susceptor, which is heated by means of an RF coil operated at 200 to 400 kHz. The RF power is monitored with a pickup coil, and the relative temperature of the susceptor is monitored by measuring the infrared emission from the susceptor that is transmitted through a fused-silica

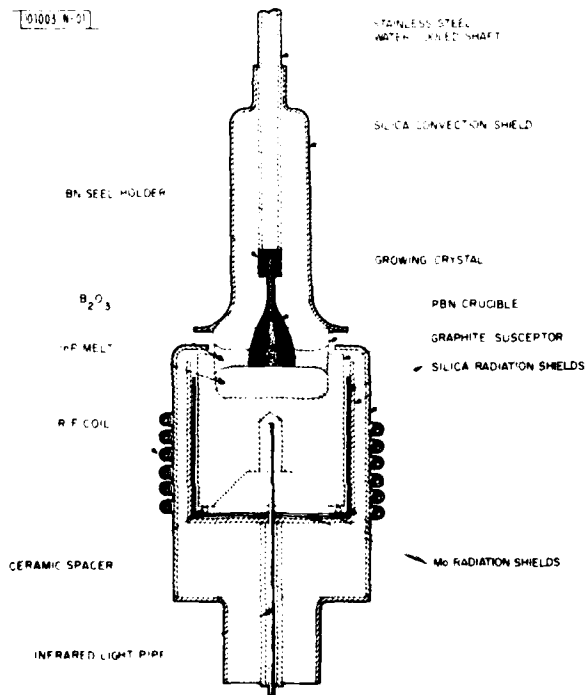


Fig. III-1. Assembly for LEC growth of InP crystals.

TABLE III-1 YIELD OF "UNTWINNED" InP BOULES OBTAINED BY STANDARD LEC GROWTH PROCEDURE		
Dopant	Number of Runs	Percentage of "Untwinned" Boules
None	4	100
Cd	4	75
Sn	4	100
Fe	9	78
Zn $< 1 \times 10^{18} \text{ cm}^{-3}$	3	100
S $< 1 \times 10^{18} \text{ cm}^{-3}$	5	80
All of the above	29	86
Zn $\geq 1 \times 10^{18} \text{ cm}^{-3}$	26	19
S $\geq 1 \times 10^{18} \text{ cm}^{-3}$	2	0

TABLE III-2 LEC GROWTH PARAMETERS THAT AFFECT TWINNING	
Growth Parameter	Change in Parameter That Reduces Twinning
Crucible Height	Decrease
B <sub>2</sub> O <sub>3</sub> Thickness	Decrease
Heat Sinking of Seed	Increase
RF Coil Position Relative to Crucible	Lower
Susceptor Height	Increase
Total Gas Pressure	Increase
Ratio of He Pressure to Ar Pressure	Increase
Pull Rate	Increase

light pipe. Fused-silica and Mo radiation shields are used to shape the temperature profile and to keep the RF coil and the walls of the pressure chamber from overheating, while a fused-silica convection shield resting on the crucible is used to reduce the convection currents in the high-pressure gas surrounding the growing crystal. The gas is a mixture of high-purity Ar and He.

Our standard LEC procedure has been used for 57 growth runs. The results obtained are summarized in Table III-1, which lists the number of runs made with each dopant and the percentage of these runs that yielded "untwinned" boules (including boules in which twinning occurred only near the lower end). A total of 29 growth runs using the standard procedure have been made either without intentional doping, with dopants other than Zn or S, or with Zn or S at concentrations below  $1 \times 10^{18} \text{ cm}^{-3}$ . These runs produced 25 untwinned boules, for an excellent overall yield of 86 percent. In striking contrast, for the 26 runs with Zn doping of  $1 \times 10^{18} \text{ cm}^{-3}$  or higher the yield was only 19 percent. Since the probability of twinning increases as the stacking fault energy decreases, the results suggest that Zn doping of InP decreases the stacking fault energy, as has been reported for Sn doping of GaAs (Ref. 2).

There may also be a relationship between the increase in twinning due to heavy Zn doping and the observation by Seki, Watanabe, and Matsui<sup>3</sup> that doping with Zn at concentrations in the low  $10^{18} \text{ cm}^{-3}$  range permits dislocation-free InP crystals to be grown by the LEC method even at high interface temperature gradients. If there is such a relationship, heavy S doping might be expected to increase the probability of twinning, since Seki *et al.*<sup>3</sup> also observed such doping to permit the growth of dislocation-free crystals. Thus, it may be significant that twinned boules were obtained in both of the runs made with our standard procedure in which the S doping exceeded  $1 \times 10^{18} \text{ cm}^{-3}$ .

In developing the standard procedure, we made a systematic investigation of the effect of changes in the growth parameters on the probability of twinning. Table III-2 lists the parameters studied and the direction of the change in each parameter that was found to decrease the incidence of twinning. In every case, a change of the parameter in the direction listed is expected to cause an increase in temperature gradient at the crystal-melt interface. (We have not yet attempted to make any temperature gradient measurements.) For example, decreasing the crucible height increases the gradient by reducing the after-heater effect of the crucible walls that extend above the melt. In a detailed study of the LEC growth of GaP crystals, Nygren<sup>4</sup> also found that the probability of twinning was reduced by decreasing the crucible height, and he too attributed this effect to an increase in the temperature gradient. We conclude that one essential requirement for twin-free growth of InP crystals by the LEC method is that the temperature gradient must exceed some minimum value.

The results given in Table III-1 indicate that Zn doping above  $1 \times 10^{18} \text{ cm}^{-3}$  significantly increases the minimum temperature gradient required for twin-free growth. We have therefore carried out several runs with heavy Zn doping in which the growth parameters were changed in the direction expected to increase the gradient. Untwinned crystals were obtained in the two most recent runs.

To provide substrates with controlled electrical properties for device studies, InP crystals must not only be appropriately doped but also have an acceptably low concentration of residual impurities. We have monitored this concentration by periodically growing crystals without intentional doping and characterizing them by means of Hall coefficient and resistivity measurements. Table III-3 gives the results for the three most recent undoped crystals and the corresponding polycrystalline charges. All the samples are n-type. For the crystals, at 77 K the

TABLE III-3 ELECTRICAL PROPERTIES OF NOMINALLY UNDOPED InP CRYSTALS				
Crystal Number	Starting Charge		LEC Crystal	
	$n_{77}(\text{cm}^{-3})$	$\mu_{77}(\text{cm}^2\text{V}^{-1}\text{sec}^{-1})$	$n_{77}(\text{cm}^{-3})$	$\mu_{77}(\text{cm}^2\text{V}^{-1}\text{sec}^{-1})$
268	$1.2 \times 10^{15}$	$8.2 \times 10^4$	$2.8 \times 10^{15}$	$4.1 \times 10^4$
280	$1.0 \times 10^{15}$	$3.9 \times 10^4$	$3.0 \times 10^{15}$	$3.5 \times 10^4$
294	$8.1 \times 10^{14}$	$7.2 \times 10^4$	$4.0 \times 10^{15}$	$3.4 \times 10^4$

carrier concentrations range from  $2.8$  to  $4.0 \times 10^{15} \text{ cm}^{-3}$ , and the mobilities from  $4.1$  to  $3.4 \times 10^4 \text{ cm}^2\text{V}^{-1}\text{sec}^{-1}$ . In each case, the carrier concentration is significantly higher and the mobility significantly lower for the crystal than for the starting charge. Two possible sources for the additional impurities are the  $\text{B}_2\text{O}_3$  encapsulant and the grain boundaries of the charge material. The impurity concentrations in the undoped crystals are too low for reliable mass spectrographic analysis. However, we do have evidence from proton-induced x-ray analysis that one batch of  $\text{B}_2\text{O}_3$  contained about 100 ppm of Zn. Mass spectrographic analysis showed that Fe-doped crystals grown with this material as encapsulant were contaminated with Zn at levels in the  $10^{15} \text{ cm}^{-3}$  range, sufficient to make the crystals p-type instead of semi-insulating. We have recently grown a number of Fe-doped crystals in runs using uncontaminated  $\text{B}_2\text{O}_3$ . The residual impurity concentrations in these crystals must be quite low, since the crystals are semi-insulating although the charge doping was only 0.01 weight percent Fe. The low residual impurity concentrations are also evidenced by the fact that the mobilities at 300 K are all between  $3.5$  and  $4.6 \times 10^3 \text{ cm}^2\text{V}^{-1}\text{sec}^{-1}$ . The latter is the highest value so far reported for semi-insulating Fe-doped InP.

G. W. Iseler

#### B. PHASE DIAGRAM FOR LPE GROWTH OF GaInAsP LAYERS LATTICE-MATCHED TO InP SUBSTRATES

Optimum performance of optoelectronic devices incorporating GaInAsP/InP heterostructures requires that the GaInAsP layers be closely lattice-matched to InP. Although many workers have prepared lattice-matched alloy layers by liquid-phase epitaxial (LPE) growth, no comprehensive phase diagram has been published for the In-rich corner of the GaInAsP system. This report presents such a diagram, which gives liquidus and solidus isotherms for the growth of lattice-matched GaInAsP alloys on both (100) and (111)B InP substrates at temperatures from 570 to 650°C and over the whole solid composition range from InP itself to the limiting P-free ternary composition,  $\text{Ga}_{0.47}\text{In}_{0.53}\text{As}$ . These isotherms reflect a general characteristic of the deposition of GaInAsP alloys at temperatures in the range used for practical LPE growth — namely, that the alloy composition obtained by growth from a given liquid at a given temperature depends on the substrate orientation.

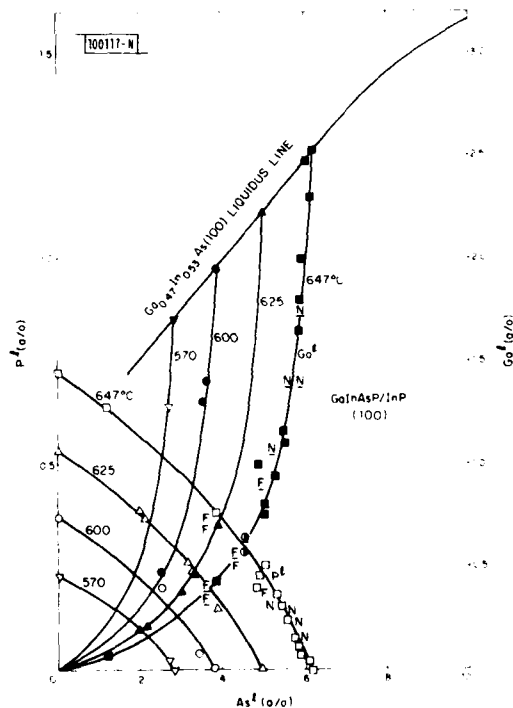
In making the phase diagram measurements, we used a horizontal graphite slider boat that was heated under flowing  $\text{H}_2$  gas in a transparent furnace, which permitted the liquidus temperatures to be determined by the direct observation method.<sup>5</sup> Accurately weighed quantities of In,

InP, InAs, and GaAs in the proportions necessary to obtain the desired liquid composition were placed in the solution well of the boat, and an oriented, polished, and etched InP wafer was placed in the substrate well. The boat was heated to a temperature high enough for the solids in the solution well to become completely molten, then cooled until some solid was formed. Next the temperature was slowly raised in small increments until the last solid just dissolved. The temperature of final dissolution was taken as the liquidus temperature.

The solidus composition was found by determining the composition of an alloy layer obtained by LPE growth from the molten solution. The boat was cooled to about 5°C below the liquidus temperature, after which the supercooled solution was pushed over the substrate, allowed to remain in contact long enough for growth of a layer 2 to 5 μm thick, and then pushed off the substrate. The composition of the layer was determined by electron microprobe analysis, and the lattice constant was found by x-ray diffractometer measurement. The liquidus temperature and solidus composition data were used in constructing the phase diagram only if the measured lattice mismatch between the layer and the InP substrate did not exceed 0.4 percent. The composition of the LPE layers depends on the amount of supercooling used, but the change in composition due to supercooling by 5°C does not exceed the uncertainty in the microprobe analysis.

The phase diagram data for the lattice-matched GaInAsP alloys are plotted in Figs. III-2 through III-5. These include the liquidus data we reported previously for InP (Ref. 6) and for  $\text{Ga}_{0.47}\text{In}_{0.53}\text{As}$  (Ref. 7). Figure III-2 shows the compositions of the liquids that yield lattice-matched alloys by growth on (100) InP substrates at four different temperatures: 570, 600, 625, and 647°C. In order to specify these liquid compositions, it is necessary to specify the content of three of the four elemental components. Therefore the results for each temperature are represented by two isotherms, which give the P content of the liquid ( $P^l$ ) and the Ga content of the

Fig. III-2. Compositions of the liquids that yield lattice-matched GaInAsP alloys by growth on (100) InP substrates at four different temperatures.



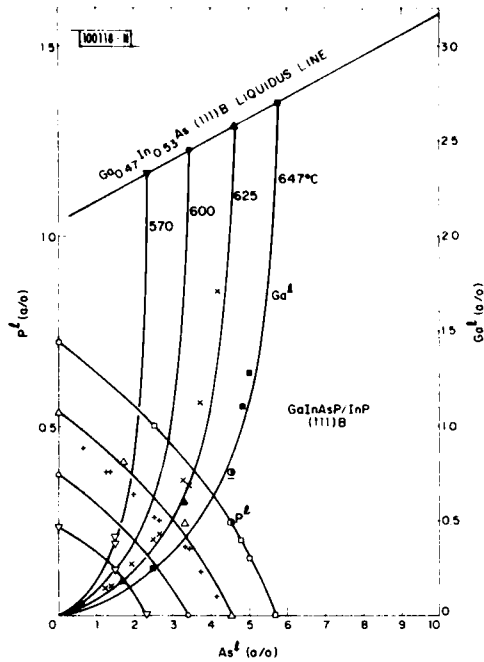


Fig. III-3. Compositions of the liquids that yield lattice-matched GaInAsP alloys by growth on (111)B InP substrates at four different temperatures.

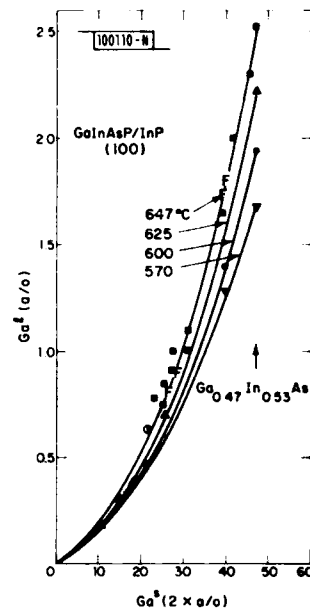


Fig. III-4. Relation between  $Ga^L$  and  $Ga^S$  for growth of lattice-matched GaInAsP alloys on (100) InP substrates at four different temperatures.

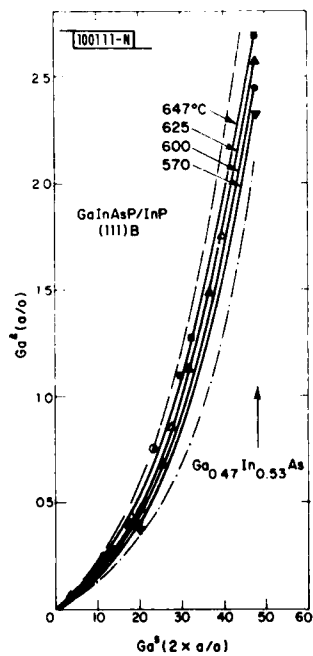


Fig. III-5. Relation between  $Ga^L$  and  $Ga^S$  for growth of lattice-matched GaInAsP alloys on (111)B InP substrates at four different temperatures.

liquid ( $Ga^l$ ), respectively, as functions of the As content of the liquid ( $As^l$ ). These isotherms have been drawn through our data points for  $P^l$  and  $Ga^l$ , which are represented in Fig. III-2 by the open and closed geometrical symbols, respectively. The  $P^l$  and  $Ga^l$  data of other authors are represented in the same figure by letters and underlined letters, respectively (F, Feng et al.<sup>8,9</sup>; N, Nagai and Noguchi<sup>10</sup>; O, Oe and Sugiyama<sup>11</sup>).

Each of the  $P^l$  isotherms in Fig. III-2 is terminated at the ordinate axis by the In-rich liquidus composition from the InP phase diagram at the isotherm temperature. Each of the  $Ga^l$  isotherms is terminated at the upper end by a point giving the composition of the P-free ternary liquid that yields  $Ga_{0.47}In_{0.53}As$  by growth at the isotherm temperature. For the region close to the ternary limit of the diagram, the liquidus temperature changes quite slowly with changing  $Ga^l$ .

Figure III-3 shows the liquidus data for the growth of lattice-matched GaInAsP alloys on (111)B InP substrates at the same four temperatures shown for (100) growth in Fig. III-2. The symbols x and +, respectively, represent the  $Ga^l$  and  $P^l$  data of Perea and Fonstad<sup>12</sup> obtained near 621°C, which are in excellent agreement with our results. Comparison of the two figures shows that for a given  $As^l$  and growth temperature the liquid yielding lattice-matched growth on (111)B substrates has a higher  $Ga^l$  and lower  $P^l$  than the liquid yielding such growth on (100) substrates.

Figure III-4 shows the relationship between the liquidus and solidus compositions for growth of lattice-matched GaInAsP alloys on (100) substrates at the four temperatures. For each temperature, this relationship is given by an isotherm obtained by simply plotting  $Ga^l$  against the Ga content in the solid ( $Ga^s$ ). This representation is possible because for a given growth temperature the liquidus composition is fixed by specifying  $Ga^l$  and using the two liquidus isotherms for that temperature shown in Fig. III-2, while the composition of a lattice-matched alloy is completely fixed by specifying the content of any one of the four elements. Each isotherm is terminated at the upper end by the point giving  $Ga^l$  for the liquid that yields  $Ga_{0.47}In_{0.53}As$ .

Figure III-5 shows the four isotherms relating  $Ga^l$  and  $Ga^s$  for lattice-matched growth on (111)B substrates. For a given  $Ga^l$ , the composition of the solid is quite insensitive to growth temperature. The dot-dashed and dashed lines are the 600 and 650°C isotherms calculated by Perea and Fonstad.<sup>12</sup> The calculation shows a larger temperature dependence than our experimental results, although the 621°C data points obtained by these authors (shown by the open triangles in the figure) are in good agreement with our experimental results. Comparison of Figs. III-4 and III-5 shows that for a given  $Ga^l$  and growth temperature the values of  $Ga^s$  and the Ga distribution coefficient ( $Ga^s/Ga^l$ ) are always higher for (100) growth than for (111)B growth, but the differences decrease with increasing temperature. This decrease in orientation dependence with increasing temperature is not surprising, since the dependence presumably results from the attachment kinetics at the growth interface or from a difference in surface energy, which becomes smaller compared to the thermal energy as the temperature increases.

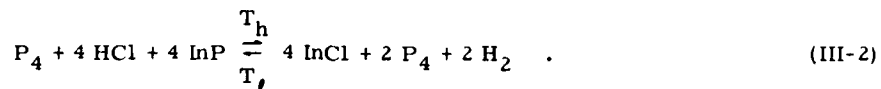
J. J. Hsieh

### C. VAPOR-PHASE EPITAXY OF GaInAsP ALLOYS ON InP SUBSTRATES

Several groups have reported vapor-phase epitaxial (VPE) growth of GaInAsP alloys on InP substrates by the hydride method, which uses  $PH_3$  and  $AsH_3$  as the sources of the Group V elements.<sup>13-16</sup> Here we describe the VPE growth of these alloys by the trichloride method, which

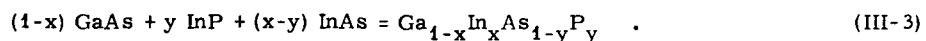
uses  $\text{PCl}_3$  and  $\text{AsCl}_3$  as the sources of these elements. The motivation for employing the trichloride method is that GaAs and InP layers of very high purity have been prepared by this technique.

The sequence of basic reactions for growing III-V compounds by the trichloride method is illustrated by the following ideal equations for InP growth:

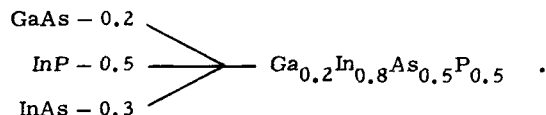


First, a Group V trichloride reacts with  $\text{H}_2$  at high temperature, yielding a gaseous mixture of the Group V element and HCl. Next, this mixture reacts with a III-V compound source at high temperature to produce a gaseous mixture of the Group III monochloride, the Group V element, and  $\text{H}_2$ . Finally, the second reaction is reversed at a lower temperature, causing deposition of the III-V compound on the substrate.

In extending the trichloride method to the VPE growth of the GaInAsP alloys, we can regard the deposition of an alloy as the deposition of a mixture of GaAs, InP, and InAs. Any alloy composition can be obtained by adjusting the relative amounts of the three compounds that are deposited on the substrate, as shown by the following equation:



For example, these amounts are as follows for an alloy that is approximately lattice-matched to InP and has its absorption edge at  $1.3 \mu\text{m}$ :



Controlling the composition deposited requires control of the composition of the gas mixture that passes over the substrate. The reactor that we use for VPE growth of GaInAsP alloys on InP substrates is designed to permit such control. Figure III-6 shows a schematic diagram of

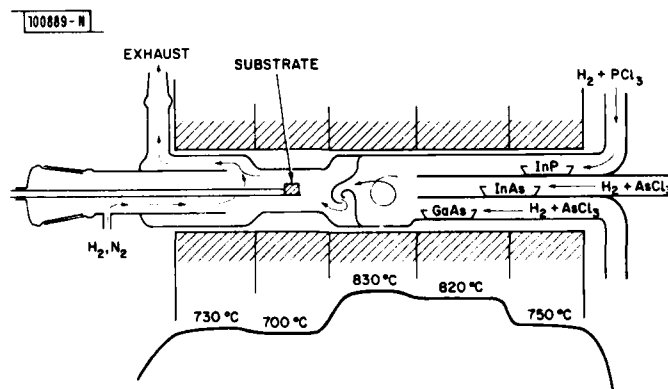


Fig. III-6. Schematic diagram of reactor and temperature profile for VPE growth of GaInAsP by trichloride transport.

this reactor, together with a representative temperature profile. The reactor uses three compound sources – InP, InAs, and GaAs – each in a separate tube. Each source is reacted with a gas mixture containing the same Group V element, which is obtained by reacting H<sub>2</sub> with either PCl<sub>3</sub> or AsCl<sub>3</sub>. The three gas streams obtained by reaction with the compound sources are combined in a high-temperature mixing chamber and then passed over the substrate, which can be inserted and removed while the reactor is at operating temperature. The composition of the combined gas stream is controlled by independently controlling the temperature and therefore partial pressure of the three trichloride reservoirs, the H<sub>2</sub> flow rate over each reservoir and its associated compound source, and the temperatures of the three sources.

Ideally, the growth conditions required for VPE growth of a particular alloy composition would be determined by the equilibria for the basic reactions of Eqs. (III-4) and (III-2). For deposition to occur, the partial pressures of the components of the vapor phase above the substrate must exceed the values in equilibrium with the alloy at the substrate temperature. For the Ga<sub>0.2</sub>In<sub>0.8</sub>P<sub>0.5</sub>As<sub>0.5</sub> alloy, these pressures are in the order InCl > P<sub>4</sub> > GaCl > As<sub>4</sub> (Refs. 17-19). In practice, the growth conditions are also influenced by a number of other factors, including the degree of completeness of the reactions between the three compound sources and the gas mixtures passing over them, changes in the composition of the final gas stream due to alloy deposition in the region of decreasing temperature between the mixing chamber and the substrate, and etching of the alloy layer by the free HCl in the final gas stream. These factors may change from run to run, reducing the reproducibility of the epilayer composition.

Under the experimental conditions used in this investigation, epilayer growth rates have generally been in the range of 1 to 3 μm/hr. The grown layers have been between 2 and 5 μm thick. Table III-4 gives the results of electrical measurements on four alloy layers with energy gaps of about 1 eV, as determined by photoluminescence measurements at room temperature. For the first layer, the resistance was too high to permit the Hall coefficient to be determined. The other three layers are n-type, with carrier concentrations at 300 K between 2.7 and 5.6 × 10<sup>16</sup> cm<sup>-3</sup> and mobilities at 77 K of 5300 to 5800 cm<sup>2</sup>V<sup>-1</sup>sec<sup>-1</sup>. Figure III-7 presents photomicrographs showing the surface morphology of three alloy layers and an InP layer grown in the same reactor. All four layers were grown on (100) InP substrates. The lattice mismatch values

TABLE III-4  
PROPERTIES OF GaInAsP EPILAYERS

Thickness (μm)	Lattice Mismatch Δa/a <sub>0</sub> (percent)	Energy Gap (eV)	Carrier Concentration (10 <sup>16</sup> cm <sup>-3</sup> )		Hall Mobility (10 <sup>3</sup> cm <sup>2</sup> V <sup>-1</sup> sec <sup>-1</sup> )	
			300 K	77 K	300 K	77 K
2.0	-0.16	1.10	-	-	-	-
2.0	-0.22	1.02	2.7	1.7	3.0	5.3
3.0	+0.31	0.99	5.6	4.5	3.5	5.8
4.0	+0.35	0.90	3.0	2.1	3.3	5.6

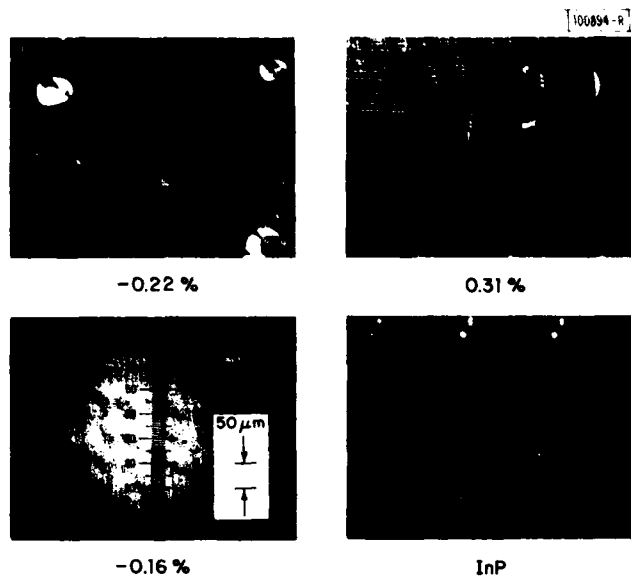


Fig. III-7. Photomicrographs of three GaInAsP layers and an InP layer grown on (100) InP substrates.

for the alloy layers are 0.32,  $-0.22$ , and  $-0.16$  percent, where a positive value indicates that the lattice constant is larger for the layer than for the substrate.

We believe that our results demonstrate the feasibility of using the trichloride method for VPE growth of GaInAsP layers on InP substrates. Further development would be required to achieve the purity and degree of composition control needed for device applications.

P. Vohl

#### D. HETEROEPITAXY OF $\text{Ge}_{1-x}\text{Si}_x$ ON Si BY TRANSIENT HEATING OF Ge-COATED Si SUBSTRATES

We recently reported<sup>20</sup> the fabrication of high-performance GaAs solar cells (with efficiencies over 20% at AML) that utilize GaAs epilayers only  $4 \mu\text{m}$  thick grown by chemical vapor deposition (CVD) on single-crystal Ge substrates. If such thin-film cells could be fabricated on Si substrates, they could be produced at much lower cost than conventional GaAs cells. However, attempts to prepare high-quality GaAs films by CVD growth directly on Si substrates have not been successful, primarily because the lattice constant of Si is about 4% smaller than that of GaAs, whereas Ge is closely lattice-matched to GaAs.

A possible solution to the problem of GaAs/Si lattice mismatch is suggested<sup>21</sup> by the fact that Si and Ge are completely miscible in the solid state, forming alloys whose lattice constants vary continuously with composition. If a Si substrate were covered with a heteroepitaxial  $\text{Ge}_{1-x}\text{Si}_x$  alloy film that was graded in composition from Si-rich at the substrate interface to Ge-rich at the front surface, the stress due to lattice mismatch might be relieved sufficiently to permit a GaAs epilayer of satisfactory crystal quality to be grown. In this report we describe the formation of heteroepitaxial  $\text{Ge}_{1-x}\text{Si}_x$  films of good quality by transient heating of Ge-coated Si substrates with a graphite strip heater. Heteroepitaxial Ge films on Si obtained by pulsed electron-beam<sup>22</sup> or laser<sup>23,24</sup> heating were found to contain rather high defect concentrations.

To prepare samples for transient heating, electron-beam evaporation or RF sputtering was used to deposit a Ge or Ge-Si film about  $0.25 \mu\text{m}$  thick on the polished surface of commercial (100) Si wafers. The wafers were cleaned by conventional procedures and rinsed with dilute HF just before loading into the deposition system. The As-deposited films were amorphous; the concentration of oxygen at the film-substrate interface was below the detection limit of Auger spectroscopy. The coated wafers were cut into individual samples with dimensions of about  $0.05 \times 1 \times 2 \text{ cm}$ .

The heating element was a graphite strip with dimensions of  $0.1 \times 6 \times 10 \text{ cm}$ . The ambient was high-purity Ar. The sample was placed at the center of the strip, usually with the Ge-coated side facing up so that the effects of heating could be observed visually. A chromel-alumel thermocouple imbedded in the strip was used to monitor the temperature. In a typical run, the temperature was raised to a maximum value ( $T_{\text{max}}$ ) of 1000 to 1100°C in about 30 sec by passing an AC current of up to 350 A through the heater strip, then lowered to room temperature at a rate of 5 to 10°C/sec.

The techniques primarily used for film characterization were reflection high-energy electron diffraction (RHEED) and x-ray diffraction. These techniques showed that if the value of  $T_{\text{max}}$  reached during heating was about 1000°C or higher the films were basically epitaxial with their single-crystal Si substrates, although regions twinned on {111} planes were present in most of the films. A few experiments with  $T_{\text{max}}$  of 800 to 900°C yielded polycrystalline films. The results obtained were similar whether the samples had been heated with the Ge-coated surface facing up or in contact with the graphite strip.

In order to determine the microtwin density in the  $\text{Ge}_x\text{Si}_{1-x}$  films, x-ray diffraction data were collected for the (311) planes. The upper trace of Fig. III-8 is a diffraction pattern showing the (311) peaks for the substrate and the epitaxial film obtained by a Bragg angle scan made on

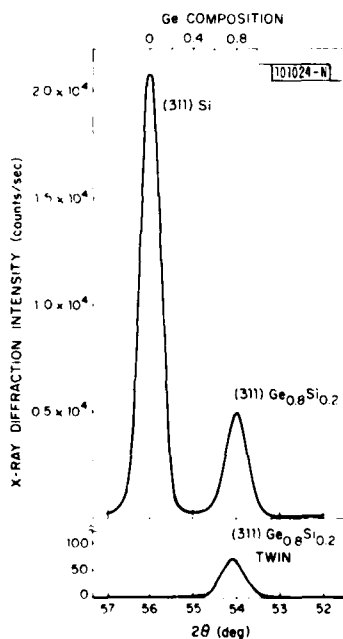


Fig. III-8. X-ray diffraction patterns for a sample prepared by transient heating of Ge-coated Si. Upper trace: (311) peaks due to Si substrate and epitaxial regions of  $\text{Ge}_{1-x}\text{Si}_x$  film. Lower trace: (311) peak due to twinned regions of  $\text{Ge}_{1-x}\text{Si}_x$  film.

a heat-treated sample. By comparing the sample orientations required to maximize each of these peaks, it was found that the difference in orientation between the film and substrate is less than  $0.5^\circ$ . From the dependence of lattice constant on composition for the  $\text{Ge}_{1-x}\text{Si}_x$  alloys,<sup>25</sup> the lattice constant obtained from the angular position of the peak for the film corresponds to a composition of  $\text{Ge}_{0.8}\text{Si}_{0.2}$ . According to the phase diagram for the Ge-Si system,<sup>26</sup> the solidus temperature for this composition is  $980^\circ\text{C}$ , close to the value of  $1000^\circ\text{C}$  for  $T_{\text{max}}$  that was reached in heat-treating the sample. Similar agreement has been found between the values of  $T_{\text{max}}$  used in other heating runs and the solidus temperatures for the  $\text{Ge}_{1-x}\text{Si}_x$  compositions obtained. For several heat-treated samples, Auger electron spectroscopy has been used to measure the  $\text{Ge}_{1-x}\text{Si}_x$  composition as a function of depth. In each case, there was an essentially uniform region adjacent to the surface for which the measured composition was close to the value determined from the x-ray diffraction data. Below this, the Ge content gradually decreased to zero over a distance of about  $1/3$  to  $1/2$  the total thickness of the film.

After making an angle scan with the sample oriented to maximize the (311) peak for the epitaxial regions of the film (in Fig. III-8, the upper trace), the sample was tilted by  $20^\circ$  toward a {111} plane in order to maximize the (311) peak for the twinned regions. The angle scan was then repeated. The lower trace in Fig. III-8 was obtained in this manner. The (311) peak appears in this trace at the same angular position as in the upper trace, since the alloy composition is the same for the twinned and epitaxial regions, but the intensity is almost two orders of magnitude lower. (There is no peak at the angular position for Si, since the substrate was untwinned.) The ratio of the (311) peak intensities for the twinned and epitaxial regions, which we call the twin index (TI), is a measure of the microtwin density. Our detection limit for TI is about  $2 \times 10^{-4}$ , corresponding to a value of about  $6 \times 10^{-4}$  for the volume fraction of twins.

In Fig. III-9, the TI values for a number of  $\text{Ge}_{1-x}\text{Si}_x$  films are plotted against the values of  $x$  determined by x-ray diffraction. The data were obtained for samples cut from four different

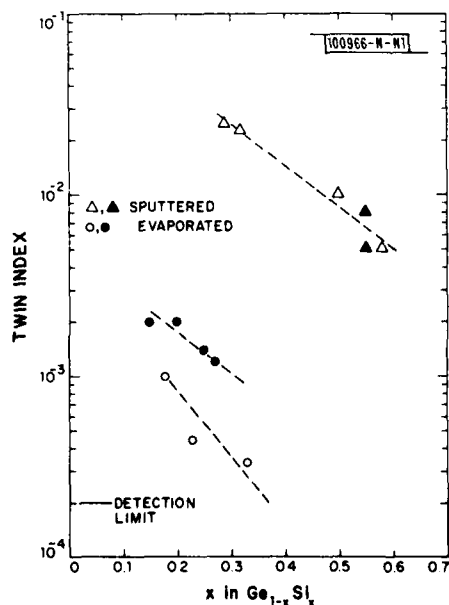


Fig. III-9. Twin index (TI) as a function of  $x$  for  $\text{Ge}_{1-x}\text{Si}_x$  films obtained by transient heating of samples from four Ge-coated Si wafers.

Si wafers, two initially coated with Ge by e-beam evaporation and the other two coated with sputtered Ge-Si containing about 10 a/o Si. Films with different values of  $x$  were obtained by using different values of  $T_{\max}$  in the heating runs. Two major trends are apparent in Fig. III-9. The TI values are much lower for samples that were initially coated with evaporated films than for those with sputtered films. The relatively poor quality of the samples with sputtered films may be due to interference with the crystallization process by Ar gas trapped in these films during deposition. Such interference has been reported previously.<sup>27</sup> Second, for samples from the same wafer the value of TI decreases as  $x$  increases, as might be expected because of the decrease in lattice mismatch between the  $\text{Ge}_{1-x}\text{Si}_x$  film and the Si substrate with increasing  $x$ . For the best of the evaporated samples, with  $x = 0.43$ , the value of TI was below our limit of detection.

Rutherford backscattering in the channeling mode has also been used to characterize several of the  $\text{Ge}_{1-x}\text{Si}_x$  films obtained by heating samples coated with evaporated Ge films. In all cases, the channeling yield was consistent with the epitaxial character of the films. The data obtained so far indicate a correlation between channeling yield and TI. For the best sample, the channeling yield was only 6 percent, for scattering from a level close to the front surface of the film, compared with the theoretical value of about 3 percent for a perfect Ge crystal. The percentage increased to 30 percent at the film/substrate interface. These results are somewhat better than the best reported for films prepared by pulsed-beam annealing.<sup>23,24</sup> Examination of our films by optical and transmission electron microscopy have not revealed the cellular structure reported in Ref. 24.

Since we have succeeded in obtaining  $\text{Ge}_{1-x}\text{Si}_x$  heteroepitaxial films of good quality by transient heating, we are now using these films as substrates for the CVD growth of GaAs layers. The initial GaAs layers are also of good epitaxial quality, with channeling yields as low as 7 percent. At this time we see no serious obstacles to the fabrication of high-efficiency GaAs solar cells using the GaAs/ $\text{Ge}_{1-x}\text{Si}_x$ /Si structure.

J. C. C. Fan    F. M. Davis  
R. P. Gale    G. H. Foley

#### E. LIQUIDUS ISOTHERMS, SOLIDUS LINES, AND LPE GROWTH IN THE Te-RICH CORNER OF THE Hg-Cd-Te SYSTEM

Liquidus isotherms and solidus lines for the  $\text{Hg}_{1-x}\text{Cd}_x\text{Te}$  primary phase field in the Te-rich corner of the Hg-Cd-Te ternary system have been obtained for temperatures from 425 to 600°C. These isotherms and lines were used to help establish conditions for the open-tube liquid phase epitaxial (LPE) growth of  $\text{Hg}_{1-x}\text{Cd}_x\text{Te}$  layers on  $\text{CdTe}_{1-y}\text{Se}_y$  substrates.

The curves of Fig. I-9 of Ref. 28, along with some additional data which were obtained by a modified direct observational technique (MDO), have been used to obtain liquidus isotherms for the Te-rich corner of the Hg-Cd-Te ternary system at temperature intervals of 25°C between 425 and 600°C. These isotherms, which are plotted as solid lines in Fig. III-10, specify the compositions of  $(\text{Hg}_{1-z}\text{Cd}_z)_{1-y}\text{Te}_y$  liquids that are in equilibrium with solid  $\text{Hg}_{1-x}\text{Cd}_x\text{Te}$ . Each isotherm is a plot of the atomic fraction of Hg,  $(1-z)(1-y)$ , as a function of the atomic fraction of Cd,  $z(1-y)$ , for these liquids at one of the selected temperatures. It is seen that at constant Hg content the solubility of Cd increases with increasing liquidus temperature ( $T_l$ ). Also, for constant  $T_l$  the solubility of Cd has a maximum with respect to changes in the Hg content. The dashed curves in Fig. III-10 are solidus lines, which are discussed below.

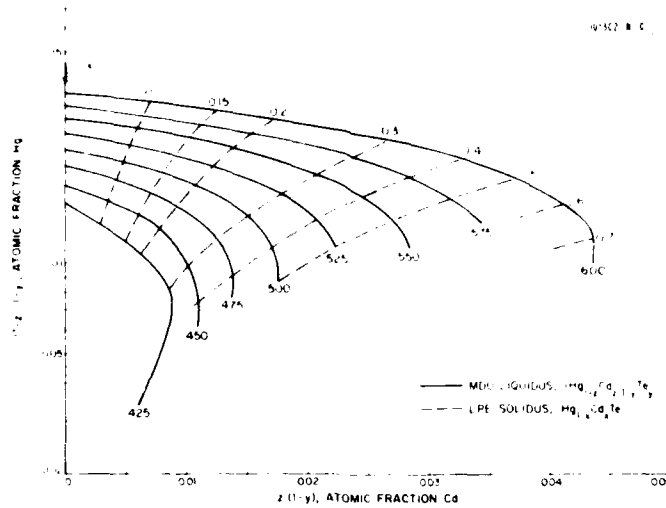


Fig. III-10. Some liquidus isotherms and solidus lines for the Te-rich corner of the Hg-Cd-Te system.

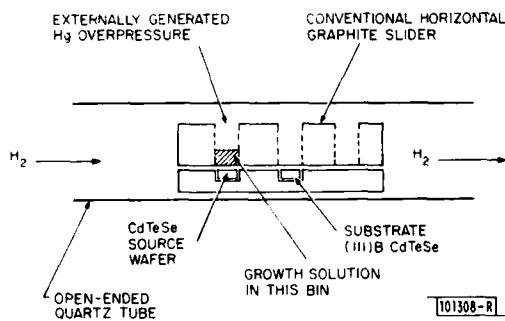


Fig. III-11. Schematic diagram of a section of the apparatus used for the open-tube liquid phase epitaxial growth of  $Hg_{1-x}Cd_xTe$  layers on  $CdTe_{1-y}Se_y$  substrates.

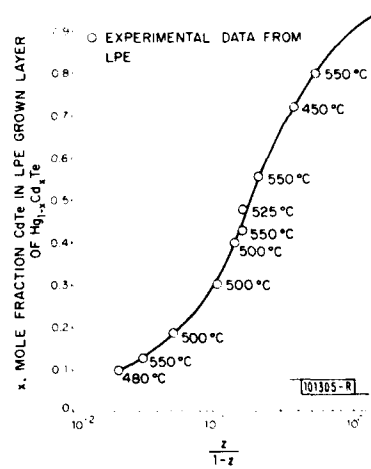


Fig. III-12. The mole fraction of CdTe,  $x$ , in the LPE-grown  $Hg_{1-x}Cd_xTe$  layer vs the atomic ratio of Cd to Hg,  $z/(1-z)$ , in the growth solution.

The LPE growth of  $\text{Hg}_{1-x}\text{Cd}_x\text{Te}$  layers from Te-rich solutions was carried out in a horizontal open tube system, using a graphite growth boat. As shown schematically in Fig. III-11, the boat consists of a lower sliding member with two 4- x 10-mm wells for  $\text{CdTe}_{1-y}\text{Se}_y$  source and substrate wafers and an upper member with 9 mm-dia. growth solution bins. To prepare growth solutions of a given composition, about 40 g of a mixture of Hg, Cd, and Te in the desired proportions was placed in a quartz ampoule, which was then evacuated and sealed, heated to 650°C for 1 to 7 days to react the elements and homogenize the melt, and rapidly cooled to room temperature to form a quenched ingot.

For each growth run the graphite boat was loaded by placing about 4.5 g of material from the quenched source ingot in the first solution bin, a wafer of CdTeSe (or CdTe) in the source well, and a single crystal wafer of CdTeSe (or CdTe) composition in the substrate well. The highest quality LPE layers were obtained by growth on (111)A- or (111)B-oriented substrates. No improvement in layer quality was achieved by using lattice-matched  $\text{CdTe}_{1-y}\text{Se}_y$  substrates instead of CdTe substrates. The loaded boat was placed in the quartz growth tube, as shown in Fig. III-11, and a flow of  $\text{H}_2$  from a Pd diffusion purifier was passed through the tube and out of the system through an oil bubbler. Before reaching the boat, the  $\text{H}_2$  stream flowed over a reservoir of liquid Hg that was maintained throughout the run at a temperature that established a partial pressure of Hg vapor (less than 1 atm) sufficient to prevent the loss of Hg from the growth solution by evaporation.

The boat was heated in ~10 min. from room temperature to an equilibration temperature of ~550°C. The source wafer was then placed under the solution bin (the position shown in Fig. III-11), and the equilibration temperature was maintained for a time, typically 60 min., long enough to insure formation of a homogeneous growth solution that was saturated by contact with the source. The source wafer was then moved away from the solution bin and cooling was begun, usually by shutting off the power to the furnace. Growth was initiated by bringing the substrate into contact with the solution at temperatures from 550 to 450°C, corresponding to solution supercooling of 0 to 100°C. For the (111)A and (111)B substrate orientations the amounts of supercooling were typically 10 and 25°C, respectively. Depending on the growth parameters and layer thickness desired, the substrate and solution were kept in contact for growth times from 15 sec to 10 min., during which cooling was continued. The decrease in temperature during these times was generally between 1 and 15°C. Growth was terminated by moving the substrate away from the solution bin and then moving the furnace away from the boat, causing rapid cooling to room temperature. The grown layers range in thickness from 3 to 15  $\mu\text{m}$ .

The alloy composition data obtained by electron microprobe analysis of  $\text{Hg}_{1-x}\text{Cd}_x\text{Te}$  layers grown by LPE from  $(\text{Hg}_{1-z}\text{Cd}_z)_{1-y}\text{Te}_y$  solutions have been used to obtain solidus data for the Te-rich corner of the Hg-Cd-Te system. For a number of growth runs, the measured mole fraction of CdTe,  $x$ , in the LPE layer is plotted in Fig. III-12 against the atomic ratio of Cd to Hg,  $z/(1-z)$ , in the growth solution. The solution composition was taken to be the same as the weighed-out composition for the quenched ingot used to load the solution bin, since the Hg partial pressure was adjusted to prevent a change in solution composition during the run.

All the points in Fig. III-12 can be represented by a single curve, although they were obtained for layers grown at temperatures over the range from 450 to 550°C. Furthermore, this liquidus-solidus curve is in good agreement with the tie-lines for the pseudobinary HgTe-CdTe system,<sup>29</sup> where  $y = 0.5$ . The insensitivity of the liquidus-solidus curve to temperature indicates that the Te-rich liquids of interest for LPE growth in the Hg-Cd-Te system behave as nearly ideal solutions.

By using the liquidus-solidus relationship given by the curve of Fig. I-3 (assumed to be independent of temperature) together with the liquidus isotherms of Fig. III-10, solidus lines have been obtained for  $\text{Hg}_{1-x}\text{Cd}_x\text{Te}$  alloys with CdTe mole fractions between 0 and 0.70. These lines are plotted as dashed lines in Fig. III-10. Each intersection of one of these solidus lines with a liquidus isotherm gives the composition of the liquid that is in equilibrium at the isotherm temperature with solid  $\text{Hg}_{1-x}\text{Cd}_x\text{Te}$  having the  $x$  value specified for the solidus line. It is seen from Fig. III-10 that a very wide range of alloy compositions can be grown in the convenient LPE growth temperature range of 425 to 600°C.

T. C. Harman

#### REFERENCES

1. H. Gottschalk, G. Patzer, and M. Alexander, *Phys. Status Solidi A* **45**, 207 (1978).
2. V. M. Astakhov, I. F. Vasileva, Yu. G. Sidorov, and S. I. Tenin, *Fiz. Tverd. Tela* **22**, 477 (1980).
3. Y. Seki, H. Watanabe, and J. Matsui, *J. Appl. Phys.* **49**, 822 (1978).
4. S. F. Nyerer, *J. Cryst. Growth* **19**, 21 (1973).
5. J. J. Hsieh, Solid State Research Report, Lincoln Laboratory, M.I.T. (1974:3), p. 25, DDC AD-A004595/8.
6. J. J. Hsieh, in *GaAs and Related Compounds, St. Louis 1976* (Institute of Physics, London, 1977), p. 74.
7. J. J. Hsieh, Solid State Research Report, Lincoln Laboratory, M.I.T. (1978:2), p. 25, DDC AD-A061241/6.
8. M. Feng, T. H. Windhorn, M. M. Tashima, and G. I. Stillman, *Appl. Phys. Lett.* **32**, 758 (1978).
9. M. Feng, I. W. Cook, M. M. Tashima, and G. I. Stillman, *J. Electron. Mater.* **9**, 241 (1980).
10. H. Nagai and Y. Noguchi, *Appl. Phys. Lett.* **32**, 234 (1978).
11. K. Oe and E. Sagiyama, *Appl. Phys. Lett.* **33**, 449 (1978).
12. E. H. Perera and C. G. Fonstad, *J. Appl. Phys.* **51**, 74 (1980).
13. E. Sagiyama, H. Kojima, H. Endo, and M. Shibata, *Jpn. J. Appl. Phys.* **16**, 2157 (1977).
14. G. H. Olsen, C. J. Nuese, and M. Ettenberg, *Appl. Phys. Lett.* **34**, 262 (1979).
15. H. Endo, *Jpn. J. Appl. Phys.* **18**, 2167 (1979).
16. I. Mizutani, M. Yoshida, A. Usui, H. Watanabe, T. Yuasa, and I. Hayashi, *Jpn. J. Appl. Phys.* **19**, 1445 (1980).
17. A. S. Bhalla, *J. Cryst. Growth* **47**, 43 (1972).
18. D. W. Stacy, *J. Phys. Chem. Solids* **36**, 411 (1975).
19. N. Uchida and H. Seki, *J. Cryst. Growth* **42**, 325 (1980).
20. J. C. C. Lee, C. O. Border, and B. J. Palm, *Appl. Phys. Lett.* **35**, 875 (1979).
21. J. C. C. Lee, G. W. Turner, R. P. Gale, and C. O. Border, *Conference Report of the 14th IEEE Photovoltaic Specialists Conference, San Diego, California, 1980* (IEEE, New York, 1980), p. 4162.
22. G. S. Lee, W. E. Esch, M. A. Nicolet, J. W. Mayer, J. V. Minnick, and N. R. Franketer, *Appl. Phys. Lett.* **35**, 255 (1978).

23. I. Golecki, I. F. Kennedy, S. S. Lau, J. W. Mayer, W. F. Tseng, R. C. Eckardt, and R. J. Wagner, *Thin Solid Films* **57**, 113 (1979).
24. H. J. Leamy, C. J. Doherty, K. C. R. Chiu, J. M. Poate, T. T. Sheng, and G. K. Celler, in Proceedings on Laser-Solid Interaction and Laser Processing, Boston, 1979 (to be published).
25. J. P. Dismukes, L. Ekstrom, and R. J. Paff, *J. Phys. Chem.* **68**, 3021 (1964).
26. H. Stohr and W. Klemm, *Z. Anorg. Allg. Chem.* **241**, 305 (1939).
27. S. S. Lau and W. F. Van der Weg in Thin Films - Interdiffusion and Relations, J. M. Poate, K. N. Tu, and J. W. Mayer, Eds. (Wiley, New York, 1978), Chapter 12.
28. T. C. Harman, Solid State Research Report, Lincoln Laboratory, M.I.T. (1980:2), p. 9.
29. T. C. Harman, in Physics and Chemistry of II-VI Compounds, M. Aven and J. S. Prener, Eds. (North Holland, Amsterdam, 1967), p. 785.

## IV. MICROELECTRONICS

### A. SPATIAL-PERIOD-DIVISION

We have recently developed a simple technique for exposing periodic and quasi-periodic structures which should be especially attractive for spatial periods below 100 nm.<sup>1</sup> The technique, which we call spatial-period-division, employs near-field diffraction from periodic and quasi-periodic parent masks to produce intensity patterns with spatial periods finer than the parent mask. This phenomenon was observed long ago with visible light and has been studied by several researchers.<sup>2</sup> What is new in our work is its use in microlithography, especially in conjunction with soft x-ray lithography.

The theory of spatial-period-division will be discussed in a later publication. A simple model<sup>1</sup> predicts that a mask pattern of period  $p$ , with an opening or slit of width  $< p/2$ , will give rise to an intensity pattern of period  $p/n$  at a distance from the mask,  $S = p^2/n\lambda$ , where  $\lambda$  is the wavelength of the incident radiation and  $\lambda < p$ . A plot of the calculated field intensity vs distance from a parent mask of period  $p$  is shown in Fig. IV-1. Note that the spatial-frequency-multiples have a reasonable depth of field. The intensity pattern shown was calculated as a simple superposition of plane waves diffracted from the grating.

The model was confirmed at visible wavelengths using a scaled simulation of a laboratory x-ray lithography unit. The feasibility of the technique was demonstrated at the 4.5-nm carbon K x-ray wavelength by "doubling" a 196.8-nm period grating-pattern x-ray mask to produce a 98.4-nm period pattern in PMMA. Exposure of higher spatial-frequency-multiples appears feasible, especially with a synchrotron source. If the mask introduces a phase shift such that the zero-order diffracted beam is cancelled and if  $p = 2\lambda$ , only the second spatial-frequency-multiple

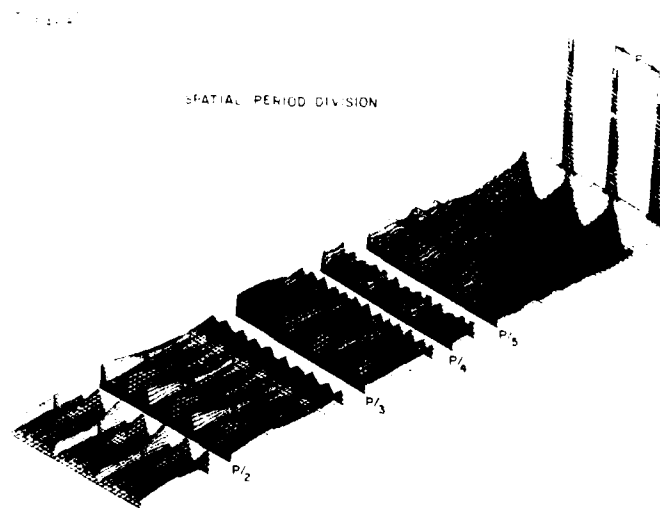


Fig. IV-1. A three-dimensional plot of the calculated near-field diffraction pattern of a "parent mask" of period  $p$  and slit width  $p/10$  is shown. The shaded sections of the plot show the intensity profile of the second, third, fourth, and fifth spatial-frequency-multiples of the parent mask at their respective distances from the parent mask.

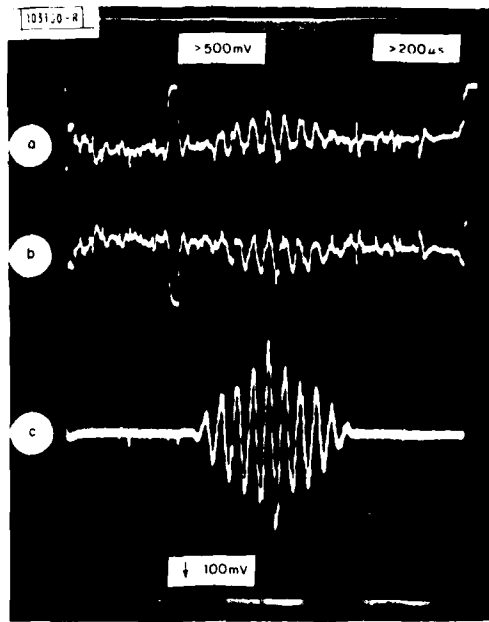


Fig. IV-2. (a) Correlator output (signal plus noise) for an input carrier frequency of 93 MHz. The signal and reference pulse widths are 0.8  $\mu$ sec. (b) Delayed output with noise inverted (signal minus noise). (c) Sum of (a) and (b).

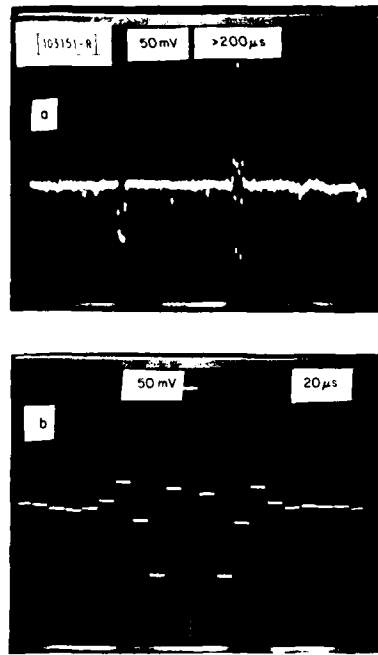


Fig. IV-3. (a) Correlator output for phase-encoded signals with 20-MHz bandwidth on an input carrier frequency of 107 MHz. (b) Expanded view of correlation peak.

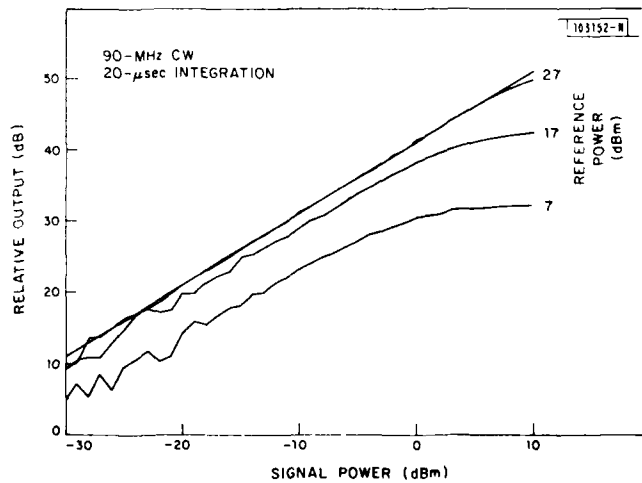


Fig. IV-4. Correlator output linearity as function of input power.

will be present. This should enable quasi-periodic patterns such as variable-period gratings and Fresnel zone plates to be "doubled."

Spatial-period-division provides a simple means of exposing large-area, low-distortion, periodic structures. It has several advantages over conventional holographic lithography. Spatial periods below 100 nm are readily exposed. When used with soft x rays, back reflection from substrates is avoided, thereby permitting high-aspect-ratio resist structures. And finally, the profile of the intensity pattern can be controlled by adjusting the slit width of the parent mask. In principle, this technique can be extended down to the limit of microlithography, which is believed to be about a 10-nm spatial period. However, fabrication of the parent mask is a challenging task.

D. C. Flanders  
A. M. Hawryluk

#### B. CHARGE-COUPLED DEVICES: SAW TIME-INTEGRATING CORRELATOR WITH CCD READOUT

We have earlier<sup>3,4</sup> described a time-integrating correlator in which the multiplication and integration of many samples of two wideband surface-acoustic wave (SAW) inputs take place in a charge-coupled device (CCD). This report describes two fixed-pattern-noise-cancellation schemes for improving the dynamic range of this device from 20 to 40 dB. One method uses a second CCD chip as an analog delay line, and the other employs digital post-processing of the CCD output. Both of these schemes take advantage of the fact that the fixed-pattern noise is time-invariant and signal-independent.

The first method of fixed-pattern-noise cancellation utilizes one of our SAW/CCD chips assembled as an analog delay line for temporary storage of the fixed-pattern noise. This pattern noise is subsequently subtracted from the active SAW/CCD output. The sequence of operation for this cancellation scheme has the correlator output with signal plus noise ( $S + N$ ) stored in the analog delay line. Then the input signal is inverted by means of a balanced mixer (a DPDT RF switch), and a second correlation is performed. *This second output is inverted* to yield signal minus noise [ $-(N - S) = (S - N)$ ] and added to the previously stored signal plus noise to produce the correlation [ $(S + N) + (S - N) = 2S$ ] shown in Fig. IV-2. This scheme provides an output in real time with the correlation output enhanced and the noise effectively suppressed.

This cancellation scheme was used to improve device performance for the correlation of 20-MHz-bandwidth pseudorandom waveforms. Figure IV-3 shows the CCD output after integrating for 200  $\mu$ sec, where Fig. IV-3(a) shows the full 3.5- $\mu$ sec correlation window stored in the CCD (including a spot defect which could have been screened out by more careful wafer testing), and Fig. IV-3(b) shows an expanded view of the correlation peak. The importance of this result is that with this real-time cancellation scheme the dynamic range of the device, as seen for the correlation peak in Fig. IV-3(b), is now sufficient to support a signal processing gain of at least 30 dB.

An A/D converter and a computer have been used to implement a digital cancellation scheme. This scheme is not limited by the noise and distortion from the analog CCD delay line of the real-time cancellation method, and can be used to determine the dynamic range of the correlator itself. Figure IV-4 shows linear response over a dynamic range in excess of 40 dB for an integration time of 20  $\mu$ sec. Similar experiments are being performed for longer integration times. These experiments are complicated by the fact that the linearity depends upon the operating

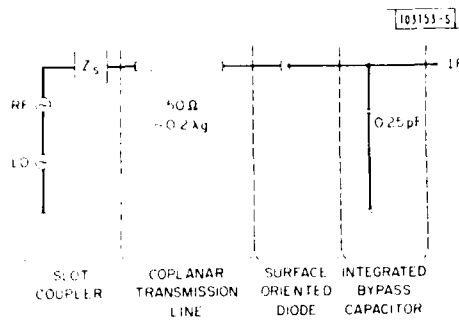


Fig. IV-5. Circuit diagram of a monolithic integrated mixer module for use at 110 GHz.

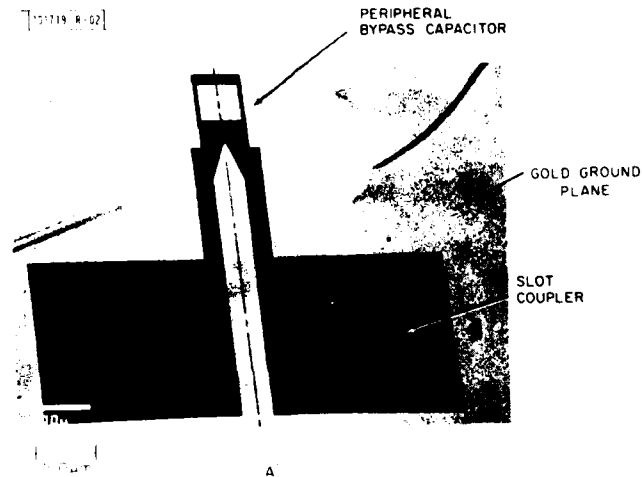


Fig. IV-6. 110-GHz monolithic integrated mixer module.

conditions of the device, and we are in the process of optimizing those operating conditions. The linear response in both integration time and signal power is necessary to achieve the desired correlation gain.

D. L. Smythe

### C. HIGH PERFORMANCE QUASI-OPTICAL GaAs MONOLITHIC MIXER AT 110 GHz

We have fabricated a novel, GaAs monolithic integrated circuit mixer which is impedance matched to fundamental waveguide. The mixer consists of a slot coupler, a coplanar transmission line, a surface-oriented Schottky-barrier diode,<sup>5,6,7</sup> and an RF bypass capacitor. All components are monolithically integrated on the GaAs surface. At 110 GHz, a monolithic mixer module mounted in the end of a waveguide horn has an uncooled double sideband (DSB) mixer noise temperature of 339 K and a conversion loss of 3.8 dB.

The method by which the signal is coupled into the mixer diode is a critical aspect of the design of an integrated mixer, especially for signals in the millimeter-wavelength regime. The coupling must be performed with low loss and by a structure which is electrically small. In this mixer, the radiation propagates through a semi-insulating GaAs slab to a slot coupler fabricated photolithographically in a metallic ground plane on the surface of the GaAs. The slot coupler is connected to a diode by an appropriate section of coplanar line, and an integrated bypass capacitor completes the mixer circuit providing a short circuit to millimeter-wave frequencies and an open circuit at the IF (Fig. IV-5). The heart of the integrated mixer circuit (Fig. IV-6) is the surface-oriented Schottky-barrier diode which is made on material having epitaxial layers of n- on n'-GaAs grown upon a semi-insulating substrate. The n'-layer is approximately 3  $\mu\text{m}$  thick with a carrier concentration of  $3 \times 10^{18} \text{ cm}^{-3}$ , while the n-layer is 0.1 to 0.2  $\mu\text{m}$  thick with a concentration 1 to  $2 \times 10^{17} \text{ cm}^{-3}$ . An alloyed Au-Ge ohmic contact region is defined on the surface of the n'-GaAs, and the Schottky-barrier metallization is a stripe of Ta-Au which is defined on the surface of the n-GaAs using optical projection lithography and metallization liftoff. Proton bombardment isolates the diode conducting area by converting epitaxial layers not used in the mixer diode to high-resistivity material. Typical parameters for the devices are junction capacitance  $C_j = 5\text{-}7 \text{ fF}$ , series-resistance  $R_s = 7 \Omega$ , and ideality factor  $n = 1.1$ . The resulting zero-bias cutoff frequency is over 3000 GHz. The Schottky-barrier metallization stripe is contacted with an overlay circuit metallization which also forms a bypass capacitor around the periphery of the ohmic contact. The module dimensions are chosen to be slightly less than the inside dimensions of WR-10 waveguide, and the module thickness is selected to suppress undesirable surface-wave modes on the GaAs.

Although each module is a complete integrated mixer, it is inconveniently small in chip form and is mounted in a larger structure (Fig. IV-7) for use. The overlay circuit ground plane metallization on the chip is alloy bonded to a ground plane metallization on the back surface of a ceramic substrate so that the ohmic contact pad (seen in Fig. IV-6) is accurately positioned over a hole drilled through the ceramic substrate. The IF signal is extracted by a TC-bonded gold ribbon which connects to a 50- $\Omega$  microstrip line defined on the front surface of the ceramic. The integrated mixer module is located in the end of a standard  $\text{TE}_{10}$  waveguide horn, and a bellows spring-contact to the microstrip line on the ceramic substrate provides an IF output connection to an OSM connector. The mixer mount is consequently rugged and mechanically simple. There is no waveguide backshort and no tuning adjustment.

The monolithic mixer module provides an impedance match to a  $\text{TE}_{10}$  wave propagating in fundamental waveguide. Therefore, the mixer module can be mounted in full-height  $\text{TE}_{10}$  waveguide and interfaced directly to any conventional waveguide component. We chose, however, a

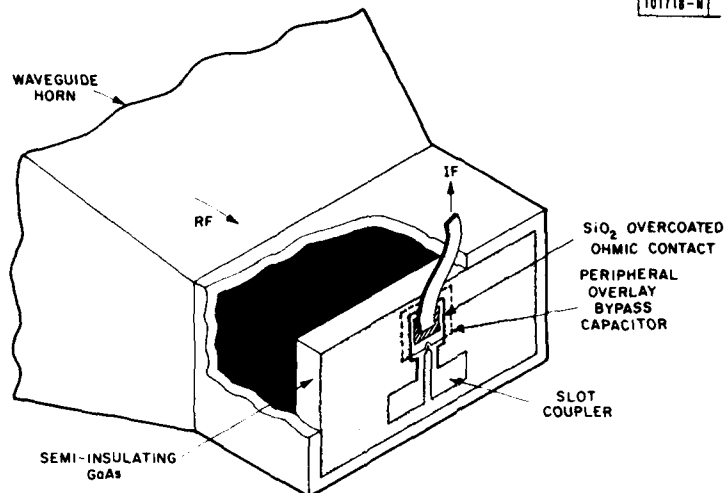


Fig. IV-7. Monolithic mixer module mounted in  $TE_{10}$  waveguide horn.

quasi-optical approach and a single-ended double-sideband receiver configuration to evaluate the monolithic mixer so that the complete receiver can be scaled to higher frequencies where waveguide techniques are inappropriate. At 110 GHz, an uncooled DSB noise temperature of 339 K and mixer conversion loss of 3.8 dB have been measured at an IF frequency of 1.2 GHz. The monolithic mixer has an inherently large RF bandwidth and should give excellent performance over the waveguide band. No RF tuning is necessary. Instantaneous bandwidth is determined by the IF matching network-IF amplifier combination. Scale-model results show that IF bandwidths greater than 6 GHz should be obtainable.

B. J. Clifton    R. A. Murphy  
G. D. Alley    I. H. Mroczkowski

#### D. LATERAL EPITAXIAL OVERGROWTH OF SILICON ON $SiO_2$

Earlier research<sup>8</sup> has shown that lines of certain materials on the surface of GaAs wafers can be embedded in a single crystal of GaAs by epitaxial growth. This work was essential for the development of the permeable base transistor (PBT)<sup>8</sup> in GaAs, and the development of a PBT in silicon will require that a similar technology be developed for embedding a grating in single-crystal silicon. We report here the lateral overgrowth of up to 4  $\mu\text{m}$  of single-crystal silicon over the edge of a thin ( $\leq 0.03 \mu\text{m}$ )  $SiO_2$  bar structure on a crystalline silicon substrate using the reduction of silane ( $SiH_4$ ) in a hydrogen-gas environment.

The test structure used to study the orientation dependence of the overgrowth phenomena is a fan-shaped pattern of 19- $\mu\text{m}$ -wide spaces etched into  $SiO_2$  or  $Si_3N_4$  and separated by nominally 95- $\mu\text{m}$ -wide lines. The spaces are directed radially at 1° angle increments from a central 1000- $\mu\text{m}$ -wide gap etched into the  $SiO_2$  or  $Si_3N_4$ . This pattern (illustrated in Fig. IV-8) was reproduced by conventional photolithographic means in films 300 Å to 1000 Å thick of both thermal  $SiO_2$  and LPCVD  $Si_3N_4$  grown on a variety of single-crystal silicon substrates. Following an acid clean, the patterned substrates were loaded on the susceptor of an induction-heated, vertical reactor, and the susceptor was heated in hydrogen. After a pre-bake to sublime native  $SiO_2$  on

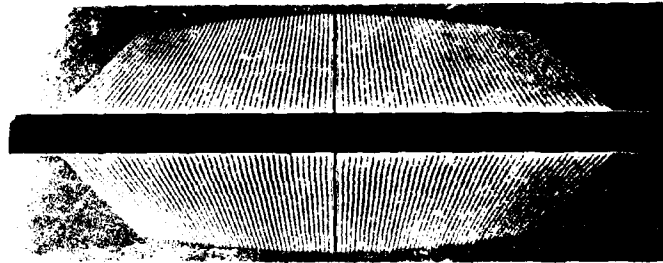


Fig. IV-8. "Fan-shaped" pattern etched in thermal  $\text{SiO}_2$  on a crystalline Si substrate. The exposed silicon lines are  $19 \mu\text{m}$  wide and are oriented at  $1^\circ$  increments. The width of oxide between adjacent lines is on the order of  $95 \mu\text{m}$ .

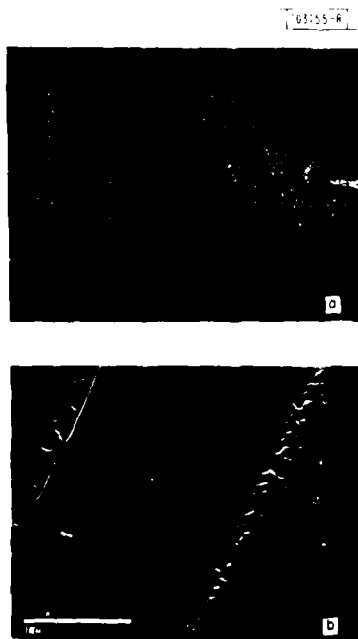


Fig. IV-9. Photomicrographs of a section of the fan pattern photolithographically engraved in  $1000 \text{ \AA}$  thermal  $\text{SiO}_2$  on (100) Si; both the optical (a) and SEM (b) pictures indicate no apparent Si overgrowth.

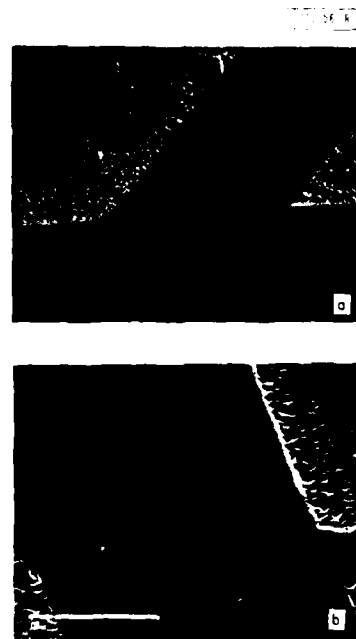


Fig. IV-10. Photomicrographs of a section of the fan pattern photolithographically engraved in  $300 \text{ \AA}$  thermal  $\text{SiO}_2$  on (100) Si. The overgrowth of epitaxial silicon over the edge of the  $\text{SiO}_2$  extends on the order of  $4 \mu\text{m}$  on the  $\text{SiO}_2$  laterally on both sides of the  $19\text{-}\mu\text{m}$ -wide pattern as seen in both the optical (a) and SEM (b) pictures.

the exposed silicon, films were deposited by the dissociation of silane at 1000°C using a source gas consisting of  $\text{SiH}_4$  in  $\text{H}_2$ . The growth rate of epitaxial silicon in the exposed portions of the substrate was approximately  $0.5 \mu\text{m}/\text{min}$ . All depositions were done using the same growth conditions.

Figures IV-9 and -10 are optical and SEM photographs of typical epitaxial depositions. The thickness of the patterned  $\text{SiO}_2$  layer is nominally 1000 Å in Fig. IV-9 and 300 Å in Fig. IV-10, and the depositions are otherwise identical. The smooth areas in the photographs are single-crystal silicon which grew up from the  $19\text{-}\mu\text{m}$ -wide spaces where the silicon substrate was exposed. The rough areas are the growth of polycrystalline silicon on the  $\text{SiO}_2$  film. For the 1000 Å oxide in Fig. IV-9, silicon-free regions are observed near the edge of the  $\text{SiO}_2$  film. In Fig. IV-10, islands of epitaxial silicon can be seen on the  $\text{SiO}_2$  where pin holes permitted the growth of epitaxial pipes showing (100) symmetry.

The amount of overgrowth is defined as the final width of the smooth epitaxial lines minus the original width ( $19 \mu\text{m}$ ) divided by 2. This assumes bilateral growth symmetry of epitaxial silicon on the oxide. For the 1000 Å oxide (Fig. IV-9), the silicon line width is nearly the same both before and after epitaxial growth, indicating no lateral overgrowth (as well as no  $\text{SiO}_2$  reduction). On the 300-Å-thick film (Fig. IV-10) as much as  $4 \mu\text{m}$  of overgrowth is observed. The results of similar depositions on patterned wafers for various combinations of  $\text{SiO}_2$  thickness and substrate orientations are summarized in Table IV-1. A wafer similarly patterned with LPCVD  $\text{Si}_3\text{N}_4$  is also listed.

One important result is the observed variation in the amount of lateral growth with amorphous film thickness. The thinner the  $\text{SiO}_2$  or  $\text{Si}_3\text{N}_4$  film, the greater the extent of lateral overgrowth. Secondly, silicon with a (100) orientation produces more overgrowth than wafers with a (111) orientation, and the (110) orientation is intermediate between the two. The angular

TABLE IV-1

Si Substrate Orientation	Amorphous Layer Type and Thickness (Å)	Lateral Overgrowth ( $\mu\text{m}$ )	Ratio of Lateral to Vertical Growth
(100)	$\text{SiO}_2$ 300	4.0	5.8
(100)	$\text{SiO}_2$ 600	1.15	2.05
(100)	$\text{SiO}_2$ 1000	~0.0	
(111)	$\text{SiO}_2$ 300+*	1.9	3.33
(110)	$\text{SiO}_2$ 300+*	2.65	4.6
(111) off 3°	$\text{SiO}_2$ 300+*	1.9	3.33
(100)	$\text{Si}_3\text{N}_4$ 300	~0.9	1.67

\* Same growth conditions as (100)  $\text{SiO}_2$ .

orientation of the spaces in the fan pattern on the wafer surface has little effect on the overgrowth of crystalline silicon for (111) and (110) silicon substrates. For (100) substrates the greatest lateral overgrowth occurs for spaces aligned 45° off the central bar, which makes them parallel to the  $\langle 100 \rangle$  direction in the surface plane. Finally, the lateral overgrowth on the  $\text{Si}_3\text{N}_4$  film was observed to be much less than that for the same thickness  $\text{SiO}_2$  film.

These results can be explained by considering the ratio of epitaxial growth rate to nucleation rate. According to Bloem,<sup>9</sup> the differences in the heterogeneous nucleation rates of silicon on various substrates are caused by differences in the degree of supersaturation required for nucleation. This supersaturation can be characterized in terms of the size of the critical cluster of silicon atoms required for nucleation, or, alternatively, the incubation time required to form the critical cluster on a given substrate. For the substrates considered in this work the relative times are  $t_{\text{SiO}_2} \sim t_{\text{Si}_3\text{N}_4} \sim t_{\text{Si-xtal}}$

The incubation period can be several seconds given appropriate deposition conditions (temperature,  $\text{SiH}_4$  partial pressure, etc.). Once deposition begins, nucleation on the exposed silicon spaces and subsequent vertical growth proceed almost immediately. If the growing silicon layer reaches the edge of the amorphous surface before nucleation has started on this surface, lateral epitaxial growth will proceed. However, shortly after nucleation commences on the  $\text{SiO}_2$  or  $\text{Si}_3\text{N}_4$ , the polysilicon crystallites quickly coalesce to cover the surface. When the amorphous surface is completely covered, lateral overgrowth of the single-crystal material stops. The lateral growth is not surprising in light of the known anisotropy of epitaxial silicon growth observed by several workers.<sup>10,11,12</sup>

From the above analysis, the lateral overgrowth would be expected to be greater for thinner  $\text{SiO}_2$  or  $\text{Si}_3\text{N}_4$  layers or for faster vertical growth rates - all other conditions being identical. This is because in both situations the lateral overgrowth will begin earlier with respect to the end of the incubation period for nucleation on the amorphous surface. This hypothesis is confirmed by the results in Table IV-1. The occurrence of maximum overgrowth on (100)-oriented silicon is explained by the fact that the epitaxial growth rate for (100) silicon is greater than that for (111) silicon because of the ease of nucleation and higher surface energy of (100) substrates.<sup>10</sup> The overgrowth observed for  $\text{Si}_3\text{N}_4$  is much smaller than that observed for an equal-thickness  $\text{SiO}_2$  film because the incubation period on  $\text{Si}_3\text{N}_4$  is shorter. Kamins and Cass<sup>13</sup> have shown that this incubation period is a strong function of temperature, silane partial pressure, and HCl content. Experiments are currently in progress to determine the effect of variations of these parameters on the lateral overgrowth.

D. D. Rathman      J. A. Burns (Group 23)  
D. J. Silversmith   C. O. Bozler

#### REFERENCES

1. D. C. Flanders, A. M. Hawryluk, and H. I. Smith, *J. Vac. Sci. Technol.* 16, 1949 (1979).
2. T. Winthrop and C. R. Worthington, *J. Opt. Sci. Am.* 55, 373 (1965).
3. Solid State Research Report, Lincoln Laboratory, M.I.T. (1979:1), DDC AD-A073152/1, pp. 51-53.
4. *Ibid.* (1980:1), pp. 32-33.
5. R. A. Murphy, C. O. Bozler, C. D. Parker, H. R. Fetterman, P. E. Tannenwald, B. J. Clifton, J. P. Donnelly, and W. T. Lindley, "Submillimeter Heterodyne Detection with Planar GaAs Schottky Barrier Diodes," *IEEE Trans. Microwave Theory Tech.* MTT-25, 494-495 (1977).
6. R. A. Murphy and B. J. Clifton, "Surface-Oriented Schottky Barrier Diodes for Millimeter and Submillimeter Wave Applications," *Proc. IEEE Intl. Electron Devices Mtg.*, Washington, D.C., 4-6 December 1978, pp. 124-128, DDC AD-A069913/2.
7. B. J. Clifton, "Schottky Diode Receivers for Operation in the 100-1000 GHz Region," *Radio and Electron. Eng.* 49, 333-346 (1979).
8. C. O. Bozler and G. D. Alley, *IEEE Trans. Electron Devices* ED-27, 1128 (1980).
9. J. Bloem, in *Proc. of the 7th Intl. Conf. on CVD*, p. 41, T. O. Sedgwick and H. Lydin, Eds. (Electrochemical Society, Princeton, N. J., 1979).
10. P. Rai-Choudhury and D. K. Schroder, *J. Electrochem. Soc.* 120, 664 (1973).
11. C. M. Drum and C. A. Clark, *J. Electrochem. Soc.* 117, 1401 (1970).
12. J. Nishizawa, Y. Kato, and M. Shimbo, *J. Cryst. Growth* 31, 290 (1975).
13. T. I. Kamins and T. R. Cass, *Thin Solid Films* 16, 147 (1973); T. I. Kamins, *IEEE Trans. Parts, Hybrids, and Packaging* PHIP-10, 221 (1974).

## V. ANALOG DEVICE TECHNOLOGY

### A. ANALOG MNOS MEMORY: MODEL AND EXPERIMENTS

In a previous report,<sup>1</sup> the concept of analog metal-nitride-oxide-semiconductor (MNOS) memory was presented and experiments demonstrating such storage in metal-gate, n-silicon-substrate MNOS capacitors were described. In the present contribution, results of a theoretical model of the MNOS analog writing process are given, and the behavior of p-silicon-substrate devices is described. The model places the concept of analog memory on a firm analytical base. The recent p-silicon results indicate that integration of the analog MNOS memory cell with a charge-coupled device (CCD) is feasible, as the MNOS and CCD processes are compatible. Such an integrated MNOS/CCD structure has been designed and is being fabricated.

Numerical results have been obtained from a model of the MNOS charge transfer process. The model includes tunneling of both majority and minority carriers. Not only are the barrier heights different for the two species, but consideration must be given to the finite number of minority carriers. The distribution of electric field is also quite different in the two cases.

Barrier heights are taken to be those given by Lundstrom and Svensson.<sup>2</sup> Majority carrier tunneling is assumed to follow the approximate modified Fowler-Nordheim expression given in the same publication. Field strengths in the oxide and nitride change as charge becomes trapped in nitride, and this is handled self-consistently. Although it is known that the trapped charge resides some tens of angstroms in the nitride,<sup>3</sup> this charge is assumed to reside at the oxide/nitride interface. This approximation is necessary unless one is willing to undertake the numerical solution of a system of partial, rather than ordinary, differential equations.

The expression for the minority carrier tunneling current density is obtained from considerations of the wavefunctions of the carriers in the inversion layer. An approximate expression which does not include the details of the energy states in the inversion layer is

$$J \approx q \sqrt{\frac{kT}{2m^*}} \frac{1}{d_{in}} n_m P_{ox} P_n$$
$$\approx \frac{q^3}{\epsilon_s \sqrt{2m^* kT}} n_m^2 P_{ox} P_n$$

where  $d_{in}$  is the inversion layer thickness,  $\epsilon_s$  the silicon dielectric constant, and  $n_m$  the surface density of minority carriers.  $P_{ox}$  and  $P_n$  are the oxide and nitride transmission probabilities given by Lundstrom and Svensson.<sup>2</sup> As with the majority carriers, the tunneled minority carriers are assumed to reside at the oxide/nitride interface. The electric field strength is calculated taking the depletion layer space charge, inversion charge, and stored charge into account.

Provision is made for the back-tunneling of trapped carriers. Different trapping energies are used in the model, but default values of 1.55 eV for electrons and 0.75 eV for holes are assumed, as given by Lundkvist *et al.*<sup>4</sup> The assumption that all carriers are trapped at the oxide/nitride interface may introduce significant error in the back-tunneling current, tending to overestimate it.

During the writing periods, back-tunneled carriers may recombine with minority carriers at the Si/SiO<sub>2</sub> interface or in the inversion layer, or they may penetrate the inversion layer and

be swept into the bulk. This process is important, since back-tunneled carriers which enter the bulk produce charge transfer without reducing the input minority charge; this could adversely affect linearity. The fraction of back-tunneled carriers which recombine with minority carriers is arbitrarily set to be some constant  $\alpha$ , where  $0 \leq \alpha \leq 1$ . Recent investigations by Schroder and White<sup>5</sup> indicate that  $0.35 \leq \alpha \leq 0.50$  for holes; for back-tunneled electrons, the results are inconclusive but could indicate  $\alpha \approx 1$ .

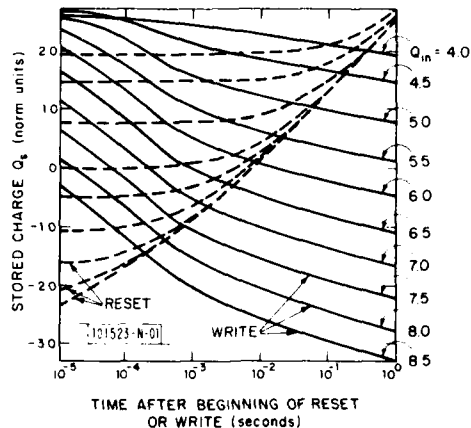
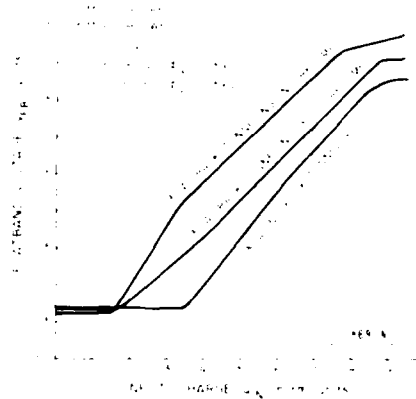


Fig. V-1. Theoretical predictions of the resetting and analog writing of an MNOS capacitor fabricated on p-silicon with 30 Å of SiO<sub>2</sub> and 500 Å of Si<sub>3</sub>N<sub>4</sub>. Reset and write voltages are -35 V and +35 V, respectively. No back-tunneling is assumed in this example. The input and stored charge are normalized so that one unit would produce a flatband shift of -5 V if stored at the SiO<sub>2</sub>/Si<sub>3</sub>N<sub>4</sub> interface. The curves are superposed on the same time scale but actually occur in the succession: reset; write with  $Q_{in} = 4.0$ ; reset; write with  $Q_{in} = 4.5$ ; reset; etc. Clearly, some writing occurs during the first  $10^{-5}$  sec of the write cycles.

Typical reset/charging characteristics for a p-substrate device are displayed in Fig. V-1. The reset/charging alternation follows the sequence: reset at -35 V for 1 sec, inject signal  $Q_{in} = 4.0$  and charge at +35 V for 1 sec, reset at -35 V, inject  $Q_{in} = 4.5$  and charge at +35 V, etc. The trapped charge  $Q_s$  is shown as a function of time for each part of the sequence. The charges  $Q_s$  and  $Q_{in}$  have been normalized such that the flatband voltage  $V_{FB}$  can be obtained by multiplying  $Q_s$  by -5 V. Note that all reset curves converge to a common value,  $Q_s = 2.7$ . More noteworthy is the fact that, for almost any time greater than 1 msec, the charging curves are spaced linearly. Thus, although the charging rate is highly nonlinear in time, the flatband voltage at any given time is a linear function of input charge. (It is evident that some charging occurs at times  $< 10 \mu\text{sec}$ , the minimum displayed.)

The data of Fig. V-2 are taken from numerical calculations such as those of Fig. V-1. These curves show the flatband voltage reached after 1 sec of reset and charging time as a function of input charge for MNOS capacitors on p-silicon with 500 Å of silicon nitride and  $\pm 35$  V applied. Results are plotted for devices with 30 Å of silicon dioxide and different assumptions about back-tunneling and Si/SiO<sub>2</sub> interfacial recombination.

Fig.V-3. Theoretical input-output relationship for the MNOS capacitor of Fig.V-1, with different assumptions of back-tunneling and Si/SiO<sub>2</sub> interfacial recombination.



A remarkable observation is that all of these input-output curves have a considerable linear dynamic range. This is, quite simply, a result of the self-limited nature of minority charge tunneling. The case with no interfacial recombination ( $\alpha = 0$ ) would be expected to show the greatest nonlinearity, as the writing process in this case is not necessarily self-limited; however, the forward electron tunneling occurs on a somewhat shorter time scale than the hole back-tunneling, so that some linearity is retained.

In all cases a certain "fat zero" level of input charge is necessary to initiate charge transfer; this is so because the oxide field  $E_{OX}$  is nearly proportional to the input charge and the tunneling  $J$  vs  $E_{OX}$  relation is highly nonlinear. Back-tunneling reduces the fat-zero level; an amount of input charge insufficient to cause its own forward tunneling may produce an oxide field sufficient to induce back-tunneling.

Nitride conduction current is not included in the model. Such current is highly nonlinear in field strength and would tend to cause saturation at both extremes of stored charge. Also not included are fixed charges in the oxide and slow surface states. These would have the effect of decreasing or increasing the fat-zero level of input charge.

All of the curves in Fig.V-2 saturate at flatband voltages somewhat higher than observed experimentally. This is likely the result of nitride conduction current which is not included in the model. Also, charge carriers, especially holes, are known to be trapped some tens of angstroms in the nitride, with the centroid of charge moving deeper as the stored charge is increased.<sup>3,6</sup> The more deeply trapped charge has less effect on the flatband voltage, so that some nonlinearity in the  $V_{FB}$  vs  $Q_{IN}$  relation will result from the increasing centroid depth.

Experiments on p-substrate MNOS capacitors have been performed in anticipation of integrating the MNOS devices with an n-channel CCD. The linearity of the analog writing process in an MNOS capacitor fabricated on 30 to 50  $\Omega$ -cm p-silicon is evident in Fig.V-3. These devices have a thermal oxide approximately 26-Å thick, a silicon nitride layer 500-Å thick deposited at 788°C, and a semitransparent chromium gate with a gold contact. The device is quite linear over the range  $-10 \leq V_{FB} \leq 0$  V and has a fat-zero input level of roughly one-third of the saturation input value. Note the relative insensitivity of the output to the write voltage.

Retention curves for this device are plotted in Fig.V-4. The retention is good, about 200 mV/decade or less over the 10-V window. (Other wafers with similar processing have had

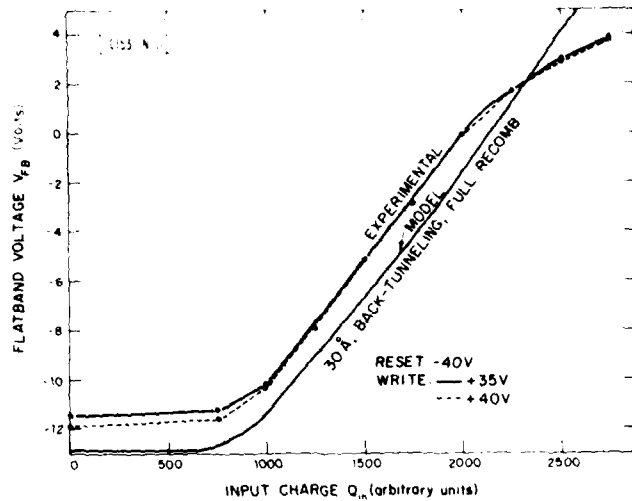


Fig.V-3. Experimental input-output relationship for an MNOS capacitor fabricated on p-silicon (wafer NM-39). Note the insensitivity of the response to the write voltage. Also shown is a theoretical curve from Fig.V-2, with the charge axis scaled to match the slope across the linear region.

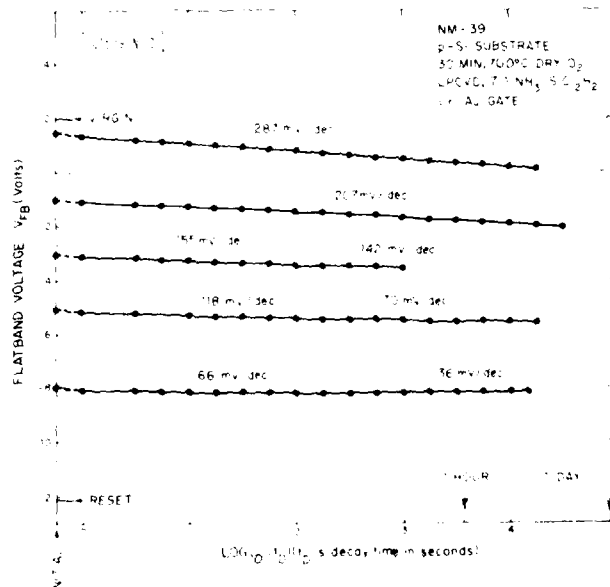


Fig.V-4. Charge retention for the device of Fig.V-3. The slopes of the decay curves are indicated.

somewhat better retention.) The interesting aspect of these charge decay curves is that they tend to converge not to a flatband voltage near zero, as is the case with n-substrate devices, but to the reset flatband voltage, about -12 V in this case. Eventually, the curves with initial flatband voltage not much less negative than the reset value do change slope and return toward zero, but this may not occur until more than  $10^5$  sec for initial flatband voltages at least 0.5 V less negative than reset. This behavior is ascribed to the fact that the holes are stored deeper in the nitride than electrons and thus back-tunnel more slowly during the writing and decay periods.

MNOS capacitors with polysilicon gates have been fabricated on p-silicon and exhibit consistently satisfactory qualities. A wafer cleaning and oxidation procedure based on a final dilute HF dip, spin dry, and immediate oxidation in dry  $O_2$  produces consistent oxide films of  $20 \pm 2$  Å. Devices with "native" oxides, with or without a water rinse before nitride deposition, demonstrate considerably poorer retention and have a memory window more negative than those of thermally oxidized devices. This is indicative of more rapid electron back-tunneling.

A mask set for a 32-sample metal- and poly-gate MNOS/CCD has been generated, and fabrication of the devices has begun. The critical steps of the required n-channel process have been satisfactorily tested by fabricating MNOS transistors.

In summary, a theoretical model has been developed which explains earlier experimental results on MNOS devices, analog memory operation has been characterized in MNOS capacitors fabricated by an n-channel CCD-compatible process, and a mask set has been produced for an integrated MNOS/CCD analog memory.

R. S. Withers  
D. J. Silversmith  
R. W. Mountain

#### B. $LiNbO_3$ SURFACE-ACOUSTIC-WAVE EDGE-BONDED TRANSDUCERS ON ST QUARTZ AND <001>-CUT GaAs

In order to generate surface acoustic waves (SAW) with wide bandwidth and low insertion loss on arbitrary substrates, many transduction methods have been tried. Edge-bonded transducers (EBT)<sup>7-11</sup> have been shown to be the best method of satisfying the above criteria. We report here experimental results using  $LiNbO_3$  for the transducer and ST quartz or GaAs for the substrate. In addition, an analytical model has been developed which gives good agreement with experimental results.

Figure V-5 shows the basic principle of operation of an edge-bonded transducer. A bulk shear-wave transducer, with polarization normal to the top surface, is bonded to a substrate on which surface waves are to propagate. Since the surface-wave particle motion is a linear combination of shear displacement normal to the surface and compressional displacement in the plane of the surface, shear waves generated in the transducer are efficiently converted to surface waves in the substrate. Only the shear-wave energy which is within about one SAW wavelength of the surface can be converted to surface waves. Thus, the top surface of the transducer and the SAW substrate must be coplanar and the back electrode which is about one SAW wavelength in height must be located at the top surface. The thickness of the shear-wave transducer determines the center frequency of operation and is approximately  $\lambda_s/2$  where  $\lambda_s$  is the shear wavelength at center frequency.

We have developed a simple model which exhibits excellent agreement with our data. This model decomposes the problem into two parts. First, the generation of bulk shear waves in the  $LiNbO_3$  transducer material is considered. Then the shear wave thus generated is converted in

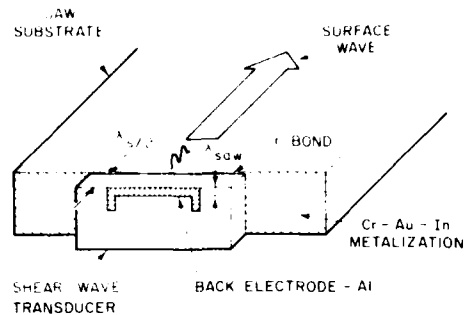


Fig. V-5. Edge-bonded transducer configuration.

the substrate material to a SAW, with conversion efficiency calculated by considering the shear energy distribution as the excitation function of an acoustic waveguide. Our model treats the  $\text{LiNbO}_3$  transducer as a conventional bulk shear-wave transducer using the standard Mason<sup>12</sup> model to calculate the electrical input impedance of the EBT using the material properties of the transducer, the bond, and the substrate. The input impedance is then used to calculate the acoustic shear-wave energy generated in the transducer (assuming no acoustic loss in the  $\text{LiNbO}_3$ ) and transmitted into the substrate. This is a straightforward application of the Mason model. The vertically polarized shear wave, which is closely confined to the surface, is then converted to a SAW whose amplitude is computed by means of an overlap integral as follows. If one assumes that the acoustic modes of the substrate are complete and orthogonal,<sup>13</sup> then the amplitude of the surface wave is given by

$$A_R = \frac{\int \vec{U}_S^*(x) \cdot \vec{U}_R(x) dx}{\int U_R^2(x) dx},$$

where  $U_R(x)$  is the surface-wave particle displacement,  $U_S(x)$  is the shear-wave particle displacement, and  $x$  is the coordinate perpendicular to the free surface. The conversion loss (in dB) of the shear-wave to surface-wave transition is given by

$$10 \log \frac{\int [A_R U_R(x)]^2 dx}{\int [U_S(x)]^2 dx}.$$

To a sufficient approximation and for ease of computation we choose

$$U_R(x) = \exp(-x/\lambda_R)$$

where  $\lambda_R$  is the SAW wavelength in the substrate and

$$U_S(x) = 1 \quad x \leq h \\ = 0 \quad x > h,$$

with  $h$  the height of the EBT electrode. When the bulk to surface-wave conversion loss is added to the electrical reflection loss computed from the Mason model, one arrives at the total EBT conversion loss.

The transducer material we have used is X-cut  $\text{LiNbO}_3$ . The transducers are bonded to the substrate with the direction of shear polarization perpendicular to the plane on which the SAW propagates.

The first step in the fabrication is the bonding of the transducer to the SAW substrate material. Cold-welded indium bonds were used because they are known to perform well in bulk-acoustic-wave devices.<sup>14</sup> The substrate for the quartz device is a 1.3-cm-thick piece of ST quartz. Following bonding the quartz substrates are cut into slices approximately 0.4 cm thick. The surface on which the SAW propagates is lapped and polished by standard techniques. Then the  $\text{LiNbO}_3$  is lapped to the desired thickness of  $\lambda_s/2$ . For the GaAs devices, the substrate is a 381- $\mu\text{m}$ -thick GaAs (<001>-cut) wafer which has been bonded to a 1.3-cm-thick piece of GaAs. Following bonding the substrate is not cut, since the wafer provides the surface on which the SAW is to propagate. The top surface of the  $\text{LiNbO}_3$  is lapped flush to the GaAs surface. Then the  $\text{LiNbO}_3$  is lapped to the desired thickness and polished.

After lapping and polishing of the  $\text{LiNbO}_3$ , the back electrode for the EBT is applied using contact printing photolithographic techniques,<sup>15</sup> followed by metallization and liftoff. Wire bonds are then made to the back electrode and to the In ground electrode.

Fig.V-6. Untuned frequency response for  $\text{LiNbO}_3$ /ST-quartz EBT: transducer thickness 13  $\mu\text{m}$ , electrode height 37  $\mu\text{m}$ , electrode width 3.18 mm.

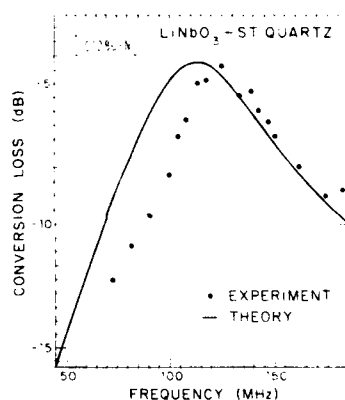


Figure V-6 shows the untuned frequency response for a typical  $\text{LiNbO}_3$  EBT on ST quartz. The parameters for this device are given in the figure caption. At 120 MHz the measured insertion loss is  $4 \text{ dB} \pm 0.5 \text{ dB}$ . The calculated curve (solid line) in Fig. V-6 is computed from the previously discussed model. The fractional bandwidth of 50% is typical for the  $\text{LiNbO}_3$ /ST-quartz structures. The center frequency of 125 MHz is the highest we have fabricated to date, and we estimate that center frequencies as high as 200 MHz may be obtained using the same fabrication methods. To reach even higher frequencies, modifications of the process by which the  $\text{LiNbO}_3$  is lapped and polished may be needed.

EBTs on GaAs have been fabricated by bonding the  $\text{LiNbO}_3$  X-cut shear-wave transducer plate on the <110> face of GaAs resulting in a piezoelectric Rayleigh wave propagating in the {110} direction on the <001> surface. The relative electric-power to acoustic-power conversion loss is shown in Fig. V-7. Here it is seen that the 3-dB fractional bandwidth is 94%, which we have found is typical of the  $\text{LiNbO}_3$ /GaAs structures. Also plotted in the same figure (solid line)

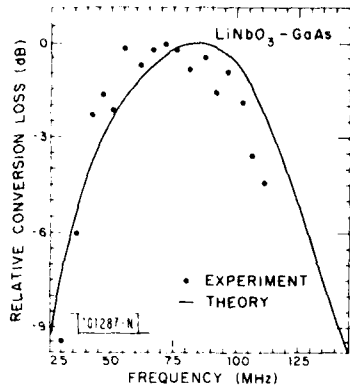


Fig. V-7. Untuned frequency response for LiNbO<sub>3</sub>/GaAs EBT: transducer thickness 20  $\mu$ m, electrode height 56  $\mu$ m, electrode width 3.48 mm.

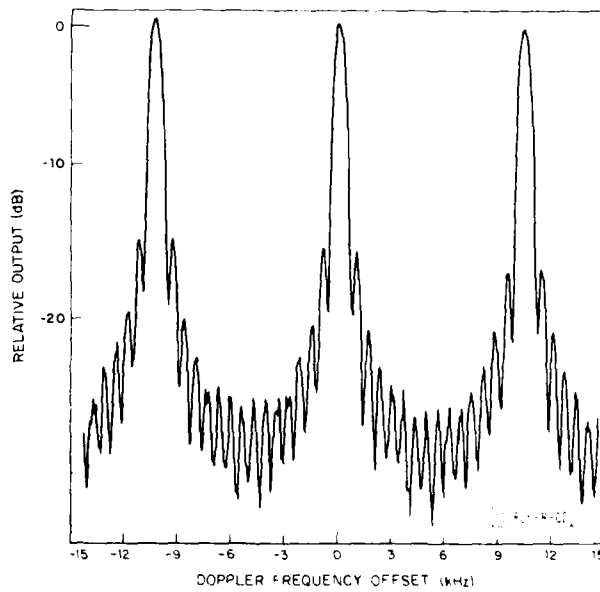


Fig. V-8. Output of coherent integrator as a function of Doppler offset frequency. The input waveform consisted of 16 3- $\mu$ sec-long gated-CW subpulses.

is the relative conversion loss predicted by the previously discussed model. The absolute conversion loss at center band is estimated to be  $11 \pm 3$  dB. This particular EBT has an 85-MHz center frequency.

Within the uncertainties of the experimental quantities the agreement between theory and measurement is very good. For the  $\text{LiNbO}_3$ /quartz device the measured conversion loss, as mentioned above, is 4 dB and this agrees well with the predicted conversion loss. The calculated center frequency for the device differs from the measurements by roughly 10 percent, which is within the uncertainties of the parameters used in the calculation.

In summary, we have fabricated  $\text{LiNbO}_3$  surface-acoustic-wave edge-bonded transducers on ST quartz and GaAs substrates which demonstrated large fractional bandwidths and low conversion losses. A theory has been developed which accurately predicts transducer performance.

D. E. Oates  
R. A. Becker  
A. C. Anderson  
R. L. Slattery  
W. C. Kernan

### C. AN ACOUSTOELECTRIC BURST-WAVEFORM PROCESSOR

A technique for processing Doppler-shifted burst waveforms with a programmable acoustoelectric coherent integrator<sup>16,17</sup> has been demonstrated. Such burst waveforms are common to many radar systems, and this demonstration indicates the feasibility of providing the important Doppler processing function in a bank of compact, low-power, coherent integrator devices.

The basic structure of the coherent integrator is illustrated in Fig. V-8. The device consists of a piezoelectric lithium niobate delay line with surface-acoustic-wave (SAW) transducers centered at frequencies of 100 and 200 MHz located at each end. The 5.5-finger-pair interdigital transducers have an aperture of 1.7 mm and a fractional bandwidth of about 20%. The evanescent electric fields associated with propagating SAWs are coupled through a uniform air-gap spacing of 350 nm to a high-density array (3.8- $\mu\text{m}$  periodicity) of PtSi-Schottky diodes on an n-type (30  $\Omega$  cm) silicon strip. The sequence of operation of the coherent integrator is as follows:

- (1) An acoustic precharge pulse centered at 200 MHz and about 100- $\mu\text{sec}$  long is applied to reverse bias the array in order to provide a linear region of operation.
- (2) A Doppler-shifted burst waveform consisting of  $N$  identical subpulses centered at 100 MHz ( $\sim 3$ - $\mu\text{sec}$  long) with about 100- $\mu\text{sec}$  subpulse repetition interval is entered into the signal port of the device. Short ( $\sim 0.1$   $\mu\text{sec}$ ) write pulses centered at 100 MHz and appropriately timed for the expected arrival of each subpulse are entered into the opposite end of the acoustic delay line. The evanescent electric field of each subpulse alone is insufficient to overcome the reverse bias of the diode array, but in combination with the write pulse each localized region of the Schottky-diode array is briefly forward biased when the write and signal waves overlap. Under suitable operating conditions this stores a linear sample of each subpulse as a spatial pattern of electrons in the diode array. Since the signal and write pulses are counterpropagating, the spatial scale of the stored charge pattern is compressed by a factor of 2. When the phase and relative timing of each write pulse

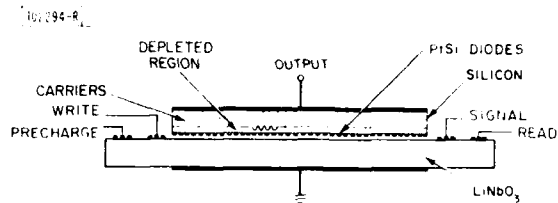


Fig. V-9. Cross-sectional view of the integrating correlator structure showing an acoustic delay line ( $\text{LiNbO}_3$ ) separated from the PtSi diode array by a narrow air gap.

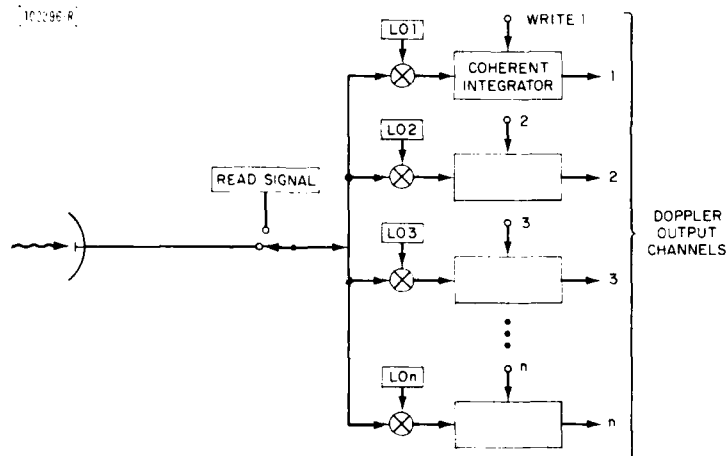


Fig. V-10. A programmable burst waveform processor with an array of coherent integrators.

is matched to the Doppler shift of the burst waveform, each of the separate subpulse charge patterns will add coherently; when burst return and write parameters are not matched, the resultant charge pattern will be smeared.

- (3) After this overlay process is accomplished, the stored charge pattern is read out by correlation with a replica of the subpulse waveform at half the time scale, that is, at 200 MHz. This results in an output corresponding to the autocorrelation of the input waveform provided the overlay charging process is linear and the write pulse has been programmed for the proper Doppler shift. The relative timing of the output provides range information. The range window is limited to 17  $\mu$ sec by the physical length of the silicon while the coherence time is limited to 20 msec by the storage time of the diodes.
- (4) After readout is completed, a brief ( $\sim 1 \mu$ sec) burst of illumination from light-emitting diodes is applied to erase the charge pattern before processing the next waveform.

To demonstrate device operation, Doppler-shifted input waveforms consisting of 2 to 32 3- $\mu$ sec-long gated-CW subpulses having about 100- $\mu$ sec intervals were employed. The output level of the coherent integrator was plotted as a function of the Doppler offset frequency of the imitated target return. The device output level for one experiment, the coherent overlay of a waveform having 16 subpulses, is shown in Fig. V-9. Note that the primary Doppler spikes are separated by an amount ( $\sim 10$  kHz) inversely proportional to the subpulse repetition interval, the number of sidelobes between the primary spikes equals the expected 14 (N-2), and the near-in sidelobe level for large N approaches the theoretically expected value of -13 dB. Similar results were obtained in the other experiments as N was varied. Experiments are currently being conducted using phase-encoded subpulses to demonstrate the full 20-MHz bandwidth capability of the device.

An array of coherent integrators could provide both Doppler and range information in a number of parallel channels, with the Doppler velocity, Doppler resolution, and range swath under programmable control. Each device, as shown in Fig. V-10, would be programmed for a different target velocity. The Doppler hypothesis is controlled by the local oscillator frequency and the timing of the write pulses applied to each integrator. The range information would appear as a time offset of the correlation peak appearing in that Doppler channel matched to the target velocity. This range resolution could be enhanced by the readout correlation process and thus is limited only by the bandwidth of the subpulse.

S. A. Reible  
I. Yao

#### REFERENCES

1. Solid State Research Report, Lincoln Laboratory, M.I.T. (1979:2), pp. 70-77, DDC AD-A078676/4.
2. K. I. Lundstrom and C. M. Svensson, *IEEE Trans. Electron Devices* ED-19, 826 (1972).
3. B. H. Yun, *Appl. Phys. Lett.* 27, 256 (1975).
4. L. Lundkvist, I. Lundstrom, and C. Svensson, *Solid-State Electron.* 16, 811 (1973).
5. D. K. Schroder and M. H. White, *IEEE Trans. Electron Devices* ED-26, 899 (1979).
6. F. L. Hampton and J. R. Cricchi, *Appl. Phys. Lett.* 35, 802 (1979).
7. C. Lardat, in 1974 Ultrasonics Symposium Proceedings (IEEE, New York, 1974), p. 433.
8. C. Lardat and P. Defranould, *Proc. IEEE* 64, 627 (1976).
9. J. E. Bowers, B. T. Khuri-Yakub, G. S. Kino and K-H Yu, in 1978 IEEE Ultrasonics Symposium Proceedings (IEEE, New York, 1978), p. 744.
10. H. C. Tuan, A. R. Selfridge, J. Bowers, B. T. Khuri-Yakub and G. S. Kino, in 1979 IEEE Ultrasonics Symposium Proceedings (IEEE, New York, 1979), p. 221.
11. W. D. Hunt, E. H. Young, and M. L. Shah, reported at the IEEE Ultrasonics Symposium, Cherry Hill, N. J., 1978 (unpublished).
12. A. H. Meitzler, in Ultrasonic Transducer Materials, edited by O. E. Maltrat (Plenum Press, New York, 1971), p. 125.
13. B. A. Auld, Acoustic Fields and Waves in Solids, Vol. II (Wiley, New York, 1973).
14. E. K. Sittig and H. D. Cook, *Proc. IEEE* 56, 1375 (1968).
15. H. I. Smith, in Surface Wave Filters, edited by H. Matthews (Wiley, New York, 1977), p. 165.
16. K. A. Ingebrigtsen and E. Stern, *Appl. Phys. Lett.* 27, 170 (1975).
17. R. W. Ralston, D. H. Hurlburt, F. J. Leonberger, J. H. Cafarella and E. Stern, in 1977 IEEE Ultrasonics Symposium Proceedings (IEEE, New York, 1977), p. 623.

UNCLASSIFIED

SECURITY CLASSIFICATION OF THIS PAGE (When Data Entered)

REPORT DOCUMENTATION PAGE		READ INSTRUCTIONS BEFORE COMPLETING FORM
1. REPORT NUMBER ESD-TR-80-151	2. GOVT ACCESSION NO. AD-A94075	3. RECIPIENT'S CATALOG NUMBER 9
4. TITLE (and Subtitle) Solid State Research	5. TYPE OF REPORT & PERIOD COVERED Quarterly Technical Summary 1 May - 31 July 1980	
	6. PERFORMING ORG. REPORT NUMBER 1980:3	
7. AUTHOR(s) Alan L. McWhorter	8. CONTRACT OR GRANT NUMBER(s) F19628-80-C-0002	
9. PERFORMING ORGANIZATION NAME AND ADDRESS Lincoln Laboratory, M.I.T. P.O. Box 73 Lexington, MA 02173	10. PROGRAM ELEMENT, PROJECT, TASK AREA & WORK UNIT NUMBERS Program Element No. 63250F Project No. 649L	
11. CONTROLLING OFFICE NAME AND ADDRESS Air Force Systems Command, USAF Andrews AFB Washington, DC 20331	12. REPORT DATE 15 August 1980	
	13. NUMBER OF PAGES 80	
14. MONITORING AGENCY NAME & ADDRESS (if different from Controlling Office) Electronic Systems Division Hanscom AFB Bedford, MA 01731	15. SECURITY CLASS. (of this report) Unclassified	
	15a. DECLASSIFICATION DOWNGRADING SCHEDULE	
16. DISTRIBUTION STATEMENT (of this Report)  Approved for public release; distribution unlimited.		
17. DISTRIBUTION STATEMENT (of the abstract entered in Block 20, if different from Report)		
18. SUPPLEMENTARY NOTES  None		
19. KEY WORDS (Continue on reverse side if necessary and identify by block number)		
solid state devices	photodiode devices	infrared imaging
quantum electronics	lasers	surface-wave transducers
materials research	laser spectroscopy	charge-coupled devices
microelectronics	imaging arrays	acoustoelectric devices
analog device technology	signal processing	
20. ABSTRACT (Continue on reverse side if necessary and identify by block number)		
<p>This report covers in detail the solid state research work of the Solid State Division at Lincoln Laboratory for the period 1 May through 31 July 1980. The topics covered are Solid State Device Research, Quantum Electronics, Materials Research, Microelectronics, and Analog Device Technology. Funding is primarily provided by the Air Force, with additional support provided by the Army, DARPA, Navy, NASA, NSF, and DOE.</p>		

Printed by  
United States Air Force  
Hanscom Air Force Base  
Bedford, Massachusetts